

EMERGENCY TRAJECTORY GENERATION FOR FIXED-WING AIRCRAFT

Saswata Paul

Submitted in Partial Fulfillment of the Requirements
for the Degree of

MASTER OF SCIENCE

Approved by:

Dr. Carlos A. Varela, Chair

Dr. Stacy E. Patterson

Dr. W. Randolph Franklin



Department of Computer Science
Rensselaer Polytechnic Institute
Troy, New York

[December 2018]

Submitted November 2018

CONTENTS

LIST OF TABLES	iv
LIST OF FIGURES	v
ACKNOWLEDGMENT	viii
ABSTRACT	ix
1. Introduction	1
1.1 Motivation	1
1.2 Contributions	2
1.3 Structure of Thesis	3
2. Dynamic Data-Driven Flight Trajectory Generation	4
2.1 Background	4
2.2 Chapter Contributions	6
2.3 Aircraft Model	6
2.3.1 Stengel’s Model	6
2.3.2 Our Extensions to Stengel’s Model for Trajectory Generation	9
2.4 Dynamic Data Driven Flight Trajectory Generation	9
2.5 Trajectory Planning Algorithm	14
2.6 Trajectory Safety Metrics	16
2.7 Experimentation and Results	18
2.7.1 Simulations With La Guardia Airport	18
2.7.2 Analysis of Alternate Landing Options for US Airways Flight 1549	25
2.7.3 Analysis of The Minimum Altitude of Return for an Airbus A320	44
3. Wind-Aware Trajectory Generation	45
3.1 Background	45
3.2 Chapter Contributions	46
3.3 Modeling the Effect of Wind on Trajectories	46
3.3.1 Effect of Wind on Turns	48
3.3.2 Effect of Wind on Straight Line Segments	49
3.4 Wind-Aware Trajectory Generation	50
3.4.1 Analytical Solution for Finding R'	52

3.4.2	Iterative Solution for Finding R'	56
3.5	Experimentation and Results	56
4.	Related Work	62
4.1	3D Trajectory Generation for Aircraft Using Dubins Curves	62
4.2	Wind Optimal Dubins 2D Paths at a Constant Altitude	62
4.3	Data Streaming and Data-Driven Avionics Systems	63
4.4	Improvements Over Existing Work	63
5.	Conclusion and Future Work	65
5.1	Conclusion	65
5.2	Future Work	66
	REFERENCES	67

LIST OF TABLES

2.1	Glide ratio and radius of turn for various bank angles at best glide speed (225 kts) for Airbus A320.	5
2.2	Glide ratio and radius of turn for various bank angles at best glide speed (65 kts) for Cessna 172.	5
2.3	US Airways 1549 relevant Flight Data Recorder data.	26
2.4	Rank of trajectories for US Airways 1549 for t+4 to t+24 seconds using glide ratio 17.25:1.	43

LIST OF FIGURES

2.1	Effect of bank angle on trajectories.	5
2.2	Position and inertial velocity of a point mass in a 3D frame.	6
2.3	Forces on a glider in straight line motion and banked turns.	7
2.4	Flowchart of dynamic data-driven approach.	10
2.5	The damaged aircraft model.	10
2.6	Estimation of glide ratio from sensors (FDR data of US Airways 1549).	11
2.7	Effect of too short size of ω	11
2.8	Effect of too large size of ω	12
2.9	Effect of too small value of σ_τ	12
2.10	Effect of too large value of σ_τ	13
2.11	Trajectories to LGA4 from an altitude of 4551 feet. New trajectories computed using data from flight simulator.	13
2.12	Flowchart of trajectory planning algorithm.	15
2.13	Low and high altitude trajectories with extended runway segments.	15
2.14	Significance of using a dirty configuration glide ratio in the final segment.	16
2.15	Trajectory to LGA4 from 4000 feet.	19
2.16	Trajectory to LGA13 from 4000 feet.	19
2.17	Trajectory to LGA31 from 4000 feet.	20
2.18	Trajectory to LGA4 from 6000 feet.	20
2.19	Trajectory to LGA13 from 6000 feet.	21
2.20	Trajectory to LGA31 from 6000 feet.	21
2.21	Trajectory to LGA4 from 8000 feet.	22
2.22	Trajectory to LGA13 from 8000 feet.	22
2.23	Trajectory to LGA31 from 8000 feet.	23
2.24	Trajectory to LGA4 from 10000 feet.	23

2.25	Trajectory to LGA13 from 10000 feet.	24
2.26	Trajectory to LGA31 from 10000 feet.	24
2.27	Flight 1549 Time vs Altitude graph.	25
2.28	Trajectory to LGA22 with a glide ratio of 17.25:1 at time $t+4$	26
2.29	Trajectory to LGA13 with a glide ratio of 17.25:1 at time $t+4$	27
2.30	Trajectory to LGA22 with a glide ratio of 17.25:1 at time $t+8$	27
2.31	Trajectory to LGA13 with a glide ratio of 17.25:1 at time $t+8$	28
2.32	Trajectory to LGA22 with a glide ratio of 17.25:1 at time $t+12$	28
2.33	Trajectory to LGA13 with a glide ratio of 17.25:1 at time $t+12$	29
2.34	Trajectory to LGA22 with a glide ratio of 17.25:1 at time $t+16$	29
2.35	Trajectory to LGA13 with a glide ratio of 17.25:1 at time $t+16$	30
2.36	Trajectory to LGA22 with a glide ratio of 17.25:1 at time $t+20$	30
2.37	Trajectory to LGA13 with a glide ratio of 17.25:1 at time $t+20$	31
2.38	Trajectory to LGA22 with a glide ratio of 17.25:1 at time $t+24$	31
2.39	Trajectory to LGA13 with a glide ratio of 17.25:1 at time $t+24$	32
2.40	Trajectory to LGA13 with a glide ratio of 17.25:1 at time $t+28$	32
2.41	Trajectory to LGA22 with a glide ratio of 19:1 at time $t+4$	33
2.42	Trajectory to LGA13 with a glide ratio of 19:1 at time $t+4$	33
2.43	Trajectory to LGA31 with a glide ratio of 19:1 at time $t+4$	34
2.44	Trajectory to LGA22 with a glide ratio of 19:1 at time $t+8$	34
2.45	Trajectory to LGA13 with a glide ratio of 19:1 at time $t+8$	35
2.46	Trajectory to LGA31 with a glide ratio of 19:1 at time $t+8$	35
2.47	Trajectory to LGA22 with a glide ratio of 19:1 at time $t+12$	36
2.48	Trajectory to LGA13 with a glide ratio of 19:1 at time $t+12$	36
2.49	Trajectory to LGA31 with a glide ratio of 19:1 at time $t+12$	37
2.50	Trajectory to LGA22 with a glide ratio of 19:1 at time $t+16$	37
2.51	Trajectory to LGA13 with a glide ratio of 19:1 at time $t+16$	38

2.52	Trajectory to LGA22 with a glide ratio of 19:1 at time $t+20$	38
2.53	Trajectory to LGA13 with a glide ratio of 19:1 at time $t+20$	39
2.54	Trajectory to LGA22 with a glide ratio of 19:1 at time $t+24$	39
2.55	Trajectory to LGA13 with a glide ratio of 19:1 at time $t+24$	40
2.56	Trajectory to LGA22 with a glide ratio of 19:1 at time $t+28$	40
2.57	Trajectory to LGA13 with a glide ratio of 19:1 at time $t+28$	41
2.58	Trajectory to LGA22 with a glide ratio of 19:1 at time $t+32$	41
2.59	Trajectory to LGA13 with a glide ratio of 19:1 at time $t+32$	42
2.60	Trajectory to LGA13 with a glide ratio of 19:1 at time $t+36$	42
2.61	Minimum altitude for returning to take-off configuration (A320).	44
2.62	Minimum altitude for returning to opposite end of runway (A320).	44
3.1	Parts of a trajectory.	47
3.2	Effect of wind on turns and straight line glide.	47
3.3	Effect of horizontal wind on glide ratio.	51
3.4	Geometry of RSR (symmetrical to LSL) and LSR (symmetrical to RSL) paths.	54
3.5	Wind-aware trajectory to LGA13 with a glide ratio of 17.25:1, 28 seconds after birds strike.	57
3.6	Wind-aware trajectory to LGA13 with a glide ratio of 19:1, 36 seconds after birds strike.	57
3.7	Effect of a 40 knot wind from different directions on a trajectory from 10000 feet.	58
3.8	Effect of different magnitudes of West-wind on a trajectory from 10000 feet.	58
3.9	Wind-aware trajectory from 5000 feet in 40 knots West-wind.	59
3.10	Wind-aware trajectory from 8000 feet in 40 knots West-wind.	59
3.11	Wind-aware trajectory from 10000 feet in 40 knots West-wind.	60
3.12	Wind-aware trajectory to LGA31 from 3850 feet, assisted by a 30 knots North-wind.	60

ACKNOWLEDGMENT

My sincere gratitude goes to my thesis advisor, Dr. Carlos Varela, for teaching me the foundations of conducting research. His invaluable guidance and constructive criticism have had an immense role in helping me complete my thesis.

I would also like to thank the rest of the members of my thesis committee: Dr. Randolph Franklin, and Dr. Stacy Patterson, for their insightful comments and feedback.

I thank all my fellow lab-mates of the Worldwide Computing Lab, especially Shigeru, Freddie, and Alexandra, who helped me in numerous ways with my research and manuscript preparation.

Sincere thanks to the National Science Foundation (NSF) and the Air Force Office of Scientific Research (AFOSR) for their financial support.

I want to express my gratitude towards my parents, whose efforts and sacrifices have shaped my life and given me all I have today. They have been the best life-coaches a person can ever hope to have.

Last, but not the least, I would like to thank my fiancé, without whose love, support and understanding it would not have been possible for me to work towards completing this thesis.

ABSTRACT

Loss of thrust emergencies, e.g. – induced by bird strikes or fuel exhaustion – give rise to the need for expeditiously generating feasible trajectories to nearby runways, in order to guide pilots. It is possible to pre-compute total loss of thrust trajectories from every point in a 3D flight plan, but dynamic factors which affect the feasibility of a trajectory, like partial power, wind conditions, and aircraft surface damage, cannot be predicted beforehand. We present a dynamic data-driven avionics software approach for emergency aircraft trajectory generation which can account for these factors. Our approach updates a damaged aircraft performance model during flight which is used for generating valid trajectories to a safe landing site. This model is parameterized on a baseline glide ratio (g_0) for a clean aircraft configuration, assuming best gliding airspeed on straight flight. The model predicts purely geometric criteria for flight trajectory generation, namely, glide ratio and radius of turn for different bank angles and drag configurations. Our model can dynamically infer the most accurate baseline glide ratio of an aircraft from real-time aircraft sensor data. We further introduce a trajectory utility function to rank trajectories for safety, in particular, to prevent steep turns close to the ground and to remain as close to the airport or landing zone as possible. Wind can significantly affect a feasible gliding trajectory with respect to the ground by changing the shape of turns from circular to trochoidal, and by increasing or decreasing the effective ground speed. Thus, in the presence of wind, otherwise feasible trajectories may become infeasible. Therefore, we present an additional wind model that takes into account the observed baseline glide ratio of an aircraft and the horizontal wind vector (\vec{w}). Our dynamic data-driven system uses this wind model to generate wind-aware trajectories that are feasible in the presence of a steady, horizontal wind. As a use case, we consider the Hudson River ditching of US Airways 1549 in January 2009, using a flight simulator to evaluate our trajectories and to get sensor data (airspeed, GPS location, and barometric altitude). In this example, baseline glide ratios of 17.25:1 and 19:1 enabled us to generate trajectories up to 28 seconds and 36 seconds after the birds strike respectively. We were also able to generate a feasible wind-assisted trajectory when trajectories were not possible in the absence of wind. In our experiments, the computation time for a single trajectory ranged from 40 milliseconds to 60 milliseconds.

CHAPTER 1

Introduction

1.1 Motivation

Aircraft loss-of-thrust (LOT) emergencies result from complete or partial loss of power in the engines and may be caused by fuel exhaustion – as in the case of Tuninter Flight-1153 [1] which ditched into the Mediterranean Sea on August 6, 2005, killing sixteen people, or bird strikes – as in the instance of US Airways Flight-1549 [2] which made an emergency landing in the Hudson River on January 15, 2009. In a total loss-of-thrust scenario, the response time is critical, and it is imperative to provide pilots with feasible trajectories to nearby runways as quickly as possible. A feasible trajectory is one which considers the actual flight capabilities of the aircraft under the emergency conditions. The choice of a feasible trajectory depends on various factors like the availability of partial power, wing surface damage, and wind conditions. Availability of partial power can affect the glide ratio of an aircraft while the presence of wind can change the shape of turns from circular to trochoidal, and affect the ground speed. While it is possible to pre-compute possible no-thrust trajectories from all points in a 3D flight-plan, it is impracticable to predict these dynamic factors in advance.

Wind has a profound effect on the shape of trajectories flown with respect to the ground, leading to significant changes in the shape and position of the resulting ground projections. Wind also affects ground-speed in a non-linear way, thus impacting the overall gliding range of an aircraft. Owing to these factors, in the presence of wind, both the horizontal and vertical profiles of a trajectory, that is valid under no-wind conditions, are significantly altered, enough to potentially render the trajectory infeasible. This calls for the need of developing an inclusive system that can quickly compute accurate trajectories by taking into account the flight capabilities of an aircraft under emergency conditions, and the horizontal wind vector (\vec{w}). Presence of such a decision support system on-board can significantly reduce the response time of pilots, thereby increasing the chances of a successful landing in the event of a loss-of-thrust emergency.

1.2 Contributions

In this thesis, we investigate the use of dynamic data-driven avionics software in decision support systems for loss-of-thrust emergency scenarios. The contributions are summarized as follows:

- We propose a dynamic data-driven trajectory generation approach that can accurately account for dynamic variables, such as partial power, wind aloft, and airplane surface damages while computing trajectories to nearby runways [3]. Dynamic Data-Driven Applications and Systems (DDDAS), used in prediction-based applications, use sensor data to dynamically update a system's model in order to improve the accuracy and effectiveness of the model [4]. Our dynamic data-driven algorithm distills a complex aerodynamic model into purely geometric constraints: glide ratio and radius of turns for different bank angles and drag configurations. Our damaged aircraft model can predict the different glide ratios and radii of turns using a single parameter: the aircraft's *baseline glide ratio*, g_0 . g_0 represents the glide ratio for a clean aircraft configuration assuming best gliding airspeed on straight flight. When g_0 is inferred from sensor data on the fly, it can be used to compute flight trajectories that automatically consider dynamic factors since their effect is reflected in the inferred value of g_0 .
- We develop *safety metrics* and compute an *utility function* to evaluate generated trajectories by considering altitude, distance from runway, bank angle over height, time of flight, extended runway length segment, and number of turns. This allows us to rank all the feasible trajectories according to the risk they impose on flights.
- We propose a wind-aware trajectory generation approach that considers a horizontal wind vector (\vec{w}) [5]. We define a wind model to predict the effect of a constant, horizontal wind on trajectories generated by our algorithm. This wind model can account for the effect of wind on ground-speed, the glide ratio with respect to the ground, and the shape of turns. Our dynamic data-driven system uses this model to predict the effect of wind and generate wind-aware trajectories that are feasible in the presence of a steady, horizontal wind.
- We use our trajectory generation algorithm to analyze alternate landing options for US Airways 1549 incident. We use data from the flight's Flight Data Recorder and try

to simulate the actual conditions of the incident as accurately as possible. We then use our safety metrics to determine what might have been the best possible option for landing the aircraft during the actual incident on January 2009.

Our work thus significantly improves upon prior Dubins based trajectory generation work by considering these data-driven geometric criteria. The aim is to reduce the response time of the pilots during an emergency by introducing automation in the decision-making phase. We used a Precision Flight Controls CAT III Flight Simulator running X-Plane software to evaluate our trajectories, and to gather sensor data (e.g., airspeed, GPS location, and barometric altitude), which we used to dynamically update the damaged aircraft performance model.

1.3 Structure of Thesis

The layout of this thesis is as follows: Chapter 2 discusses our dynamic data-driven trajectory generation approach, Chapter 3 presents our wind-aware trajectory generation approach, Chapter 4 discusses related work, and Chapter 5 concludes the thesis and explores some future directions of work.

CHAPTER 2

Dynamic Data-Driven Flight Trajectory Generation

2.1 Background

In this chapter, we present a dynamic data-driven approach for generating trajectories in the event of loss-of-thrust aircraft emergencies. Our approach generates a no-thrust trajectory with clean configuration glide ratio and then gathers sensor data from aircraft sensors for comparison. If there is an inconsistency, the observed data is sent to a *model refinement component* which infers a new *baseline glide ratio* (g_0) consistent with the observed data and sends it to the damaged aircraft model. The *damaged aircraft model* uses this refined baseline glide ratio to create a new function for computing glide ratios for different bank angles. This function is made available to the trajectory generation algorithm for generating trajectories which are consistent with the actual capabilities of the aircraft. The damaged aircraft model takes as input the glide ratio for the clean configuration and a *drag multiplier table* for generating the glide ratios in dirty configurations. It can then generate glide ratios and *radii of turn* (r) for different values of bank angle, airspeed and drag configuration. Our trajectory planning algorithm generates trajectories from an initial point to a given runway or a set of runways in case of a loss-of-thrust emergency.

In a loss-of-thrust situation, the response time is critical. Therefore, it is important for the pilots to make a quick and educated choice among all possible trajectories which are generated. To aid this, we develop certain safety metrics to rank all the computed trajectories according to the risk they might inflict. These metrics consider altitude, distance from runway, bank angle over height, time of flight, extended runway length segment, and number of turns. We define an *utility function* – a function of the weighted values of these metrics, which can be used for assigning the ranks.

Portions of this chapter have been presented as: S. Paul, F. Hole, A. Zyteck and C. A. Varela. “Flight Trajectory Planning for Fixed-Wing Aircraft in Loss of Thrust Emergencies.” in *The 2nd Int. Conf. on InfoSymbiotics / DDDAS (Dynamic Data Driven Applications Systems)*, Boston, MA, USA, August 2017.

Portions of this chapter previously appeared as: S. Paul, F. Hole, A. Zyteck, and C. A. Varela. “Wind-aware trajectory planning for fixed-wing aircraft in loss of thrust emergencies.” in *Proc. of the 37th AIAA/IEEE Digit. Avionics Syst. Conf.*, London, England, UK, September 2018, pages 558-567.

Portions of this chapter have been submitted to: S. Paul and C. A. Varela. “Data-Driven Wind-Aware Emergency Trajectory Planning for Fixed-Wing Aircraft.” in *J. Aircraft*.

Table 2.1: Glide ratio and radius of turn for various bank angles at best glide speed (225 kts) for Airbus A320.

Bank angle:	0°	10°	20°	30°	45°	60°
Glide ratio:	17.25:1	16.98:1	16.21:1	14.92:1	12.19:1	8.62:1
Radius of turn (feet):	∞	25430	12319	7766	4484	2588

Table 2.2: Glide ratio and radius of turn for various bank angles at best glide speed (65 kts) for Cessna 172.

Bank angle:	0°	10°	20°	30°	45°	60°
Glide ratio:	9:1	8.86:1	8.45:1	7.79:1	6.36:1	4.5:1
Radius of turn (feet):	∞	2122	1028	648	374	216

Bank angle of turns has a major impact on the glide ratio and radius of turn of an aircraft (Table 2.2, Table 2.1). These variations in the glide ratios and the radii of turns has a major impact on the viability of the trajectories (Fig. 2.1). Therefore, in our trajectory planning algorithm, we use three discrete values of bank angles: 20°, 30° and 45°. All the scenarios and experiments in this chapter have been simulated for an Airbus A320.

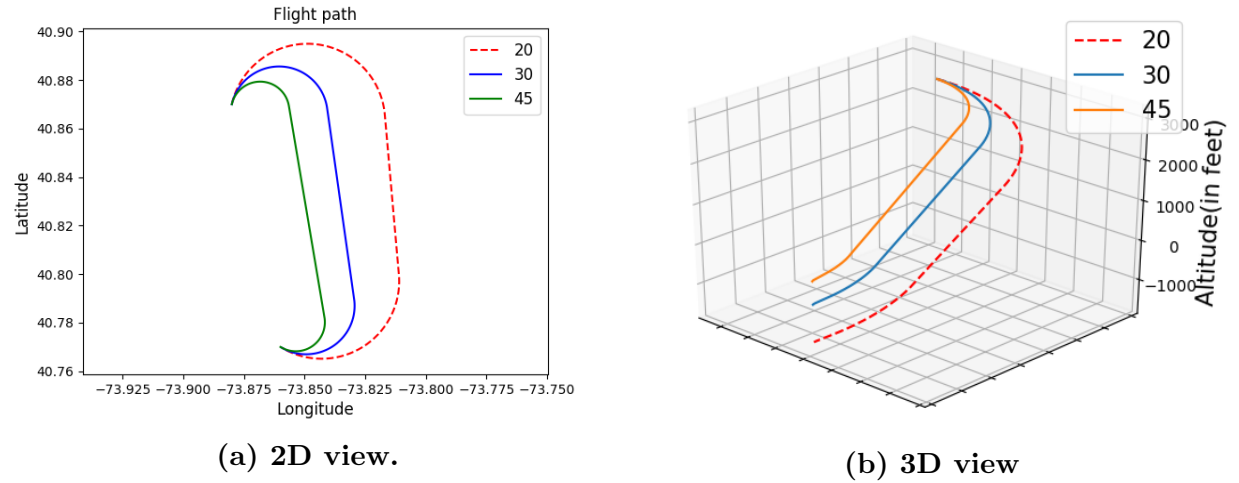


Fig. 2.1: Effect of bank angle on trajectories.

2.2 Chapter Contributions

The following items represent our original research contributions as presented in this chapter:

- Our dynamic data-driven model for trajectory generation (Section 2.4).
- Our trajectory generation algorithm (Section 2.5).
- Our safety metrics for trajectory evaluation (Section 2.6).
- Experimental evaluation of our approach and analysis of alternate landing options for US Airways flight 1549. (Section 2.7).

2.3 Aircraft Model

2.3.1 Stengel's Model

We adopted the aircraft model developed by Stengel [6]. We summarize this model in this subsection.

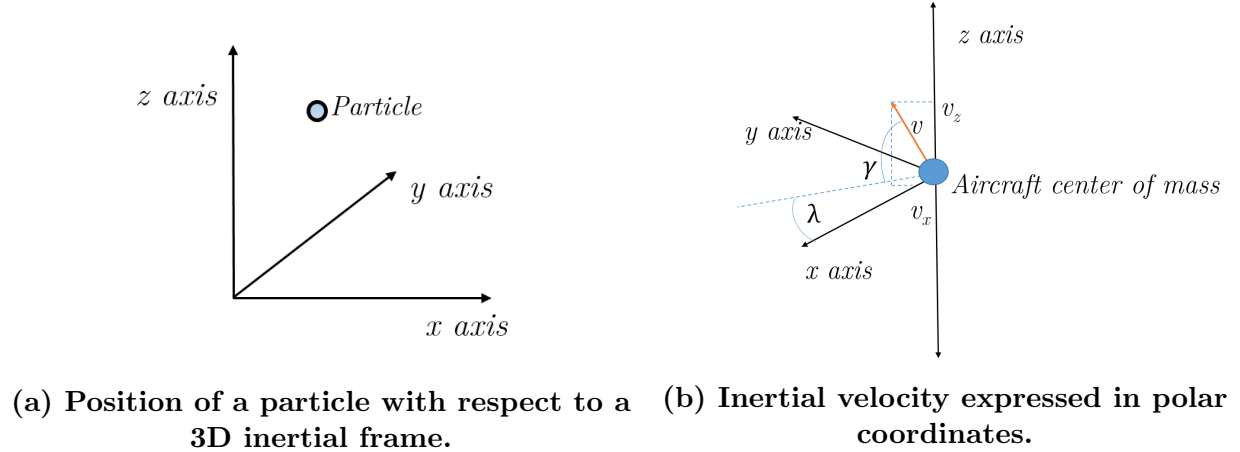


Fig. 2.2: Position and inertial velocity of a point mass in a 3D frame.

The position of a point with respect to a 3D inertial frame is given by:

$$[x \ y \ z]^\top \quad (2.1)$$

Therefore, the velocity (v) and linear momentum (p) of a particle are given by:

$$v = \frac{d[x \ y \ z]^\top}{dt} = [\dot{x} \ \dot{y} \ \dot{z}]^\top = [v_x \ v_y \ v_z]^\top \quad (2.2)$$

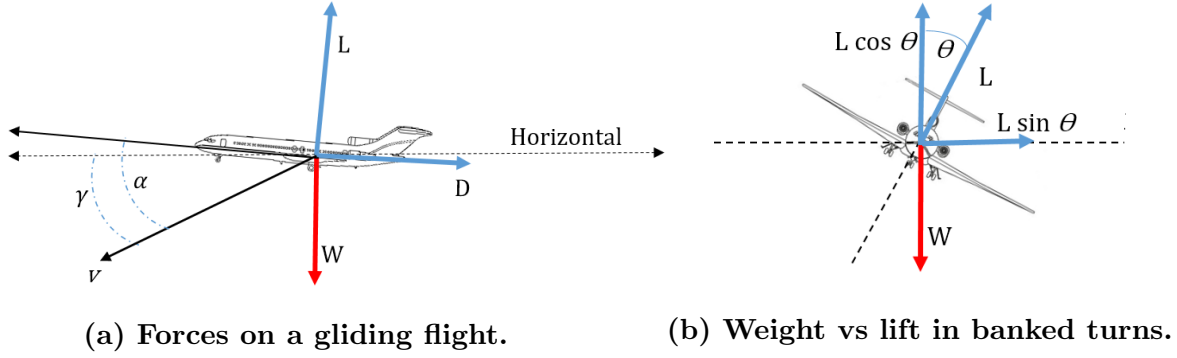


Fig. 2.3: Forces on a glider in straight line motion and banked turns.

$$p = mv = m [v_x \ v_y \ v_z]^\top \quad (2.3)$$

where m = mass of the particle. Fig 2.2b shows the inertial velocity of a point mass in polar coordinates, where γ is the vertical flight path angle and λ is the horizontal flight path angle. Considering the motion to be a straight line motion in a particular direction, we can use v_x to denote motion in the xy horizontal plane. Two dimensional equations for motion of a point mass, which coincides with the center of mass of an aircraft, restricted to the vertical plane are given below:

$$\begin{bmatrix} \dot{x} \\ \dot{z} \\ \dot{v}_x \\ \dot{v}_z \end{bmatrix} = \begin{bmatrix} v_x \\ v_z \\ f_x/m \\ f_z/m \end{bmatrix} \quad (2.4)$$

Transforming velocity to polar coordinates:

$$\begin{aligned} \begin{bmatrix} \dot{x} \\ \dot{z} \end{bmatrix} &= \begin{bmatrix} v_x \\ v_z \end{bmatrix} = \begin{bmatrix} v \cos \gamma \\ -v \sin \gamma \end{bmatrix} \\ \Rightarrow \begin{bmatrix} v \\ \gamma \end{bmatrix} &= \begin{bmatrix} \sqrt{v_x^2 + v_z^2} \\ -\sin^{-1}(v_z/v) \end{bmatrix} \end{aligned} \quad (2.5)$$

Therefore, rates of change of velocity and flight path angle are given by:

$$\begin{bmatrix} \dot{v} \\ \dot{\gamma} \end{bmatrix} = \begin{bmatrix} \frac{d}{dt} \sqrt{v_x^2 + v_z^2} \\ -\frac{d}{dt} \sin^{-1}(v_z/v) \end{bmatrix} \quad (2.6)$$

Longitudinal equations of motion for a point mass are given by:

$$\dot{x}(t) = v_x = v(t) \cos \gamma(t) \quad (2.7)$$

$$\dot{z}(t) = v_z = -v(t) \sin \gamma(t) \quad (2.8)$$

$$\dot{v}(t) = \frac{(C_T \cos \alpha - C_D) \frac{1}{2} \rho(z) v^2(t) S - mG \sin \gamma(t)}{m} \quad (2.9)$$

$$\dot{\gamma}(t) = \frac{(C_T \sin \alpha + C_L) \frac{1}{2} \rho(z) v^2(t) S - mG \cos \gamma(t)}{mv(t)} \quad (2.10)$$

where C_T is side force coefficient, C_D is drag coefficient ρ is density of air, α is the angle of attack, C_L is lift coefficient, S is the surface area of the wing and G is the gravitational constant ($11.29 \text{ kn}^2\text{ft}^{-1}$). Lift and Drag are given by $L = C_L \frac{1}{2} \rho v^2 S$, $D = C_D \frac{1}{2} \rho v^2 S$. Thus, for a gliding flight, the condition of equilibrium is defined by the following equations:

$$L = C_L \frac{1}{2} \rho v^2 S = W \cos \gamma \quad (2.11)$$

$$D = C_D \frac{1}{2} \rho v^2 S = W \sin \gamma \quad (2.12)$$

where W is the weight of the aircraft.

Therefore, the gliding flight path angle (Fig. 2.3a) can be found:

$$\cot \gamma = \frac{L}{D} \quad (2.13)$$

From equations 2.7 and 2.8, we have $\dot{x} = v \cos \gamma$, $\dot{z} = -v \sin \gamma$. Therefore,

$$\cot \gamma = \frac{\dot{x}}{-\dot{z}} = \frac{\Delta x}{-\Delta z} = g_0 \quad (2.14)$$

where g_0 is the baseline glide ratio. Hence, from equations 2.13 and 2.14, we can conclude that $g_0 = \frac{L}{D}$. Therefore, glide range is maximum when (L/D) is maximum.

2.3.2 Our Extensions to Stengel's Model for Trajectory Generation

For banked turns, if the bank angle is θ , the vertical component of lift, $L' = L \cos \theta$ (Fig. 2.3b).

$$g(\theta, k) = \frac{L'}{D} = \left(\frac{L}{D} \right) \cos \theta = g(k) \cos \theta, \text{ where } k \text{ is the drag configuration.} \quad (2.15)$$

The drag multiplier function $\delta(k)$ is a ratio that can be used to obtain the baseline glide ratio $g(k)$ for a drag configuration k from the baseline glide ratio of clean configuration g_0 .

$$g(k) = g_0 \delta(k) \quad (2.16)$$

Given the baseline glide ratio g_0 and a drag configuration k , the glide ratio for a bank angle θ can be obtained from equation 2.17.

$$g(\theta, k) = g_0 \delta(k) \cos \theta \quad (2.17)$$

Given the horizontal aircraft airspeed v_x , the radius of turn $r(\theta, v_x)$ for a bank angle θ can be obtained from equation 2.18.

$$r(\theta, v_x) = \frac{v_x^2}{G \times \tan \theta} \quad (2.18)$$

Equations 2.17 and 2.18, form the basis of our geometrical model of a gliding flight. In the rest of the chapter, we will use v to refer to v_x .

2.4 Dynamic Data Driven Flight Trajectory Generation

A flowchart of our dynamic data driven approach is given in Fig. 2.4. There are four components: the *damaged aircraft model*, *flight trajectory generator*, *aircraft/sensors* and the *model refinement component*.

The damaged aircraft model (Fig. 2.5) takes as inputs the new baseline glide ratio (g_0) and a drag multiplier function (δ). The functions for calculating the glide ratio ($g(\theta, k)$) for every bank angle (θ) (Eq. 2.17) and the corresponding radius of turn ($r(\theta, v_x)$) (Eq. 2.18) are sent from the damaged aircraft model to the flight trajectory generator to be used in the trajectory planning algorithm for computing trajectories. We constantly read data from

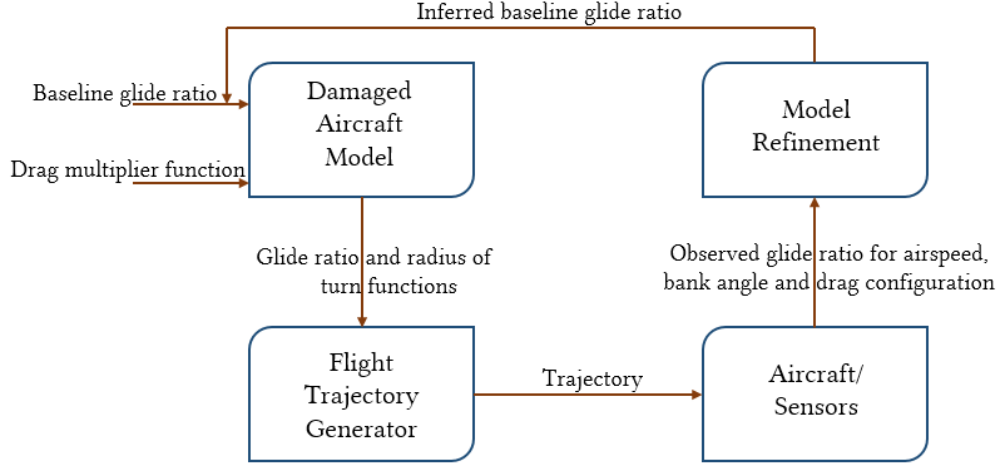


Fig. 2.4: Flowchart of dynamic data-driven approach.

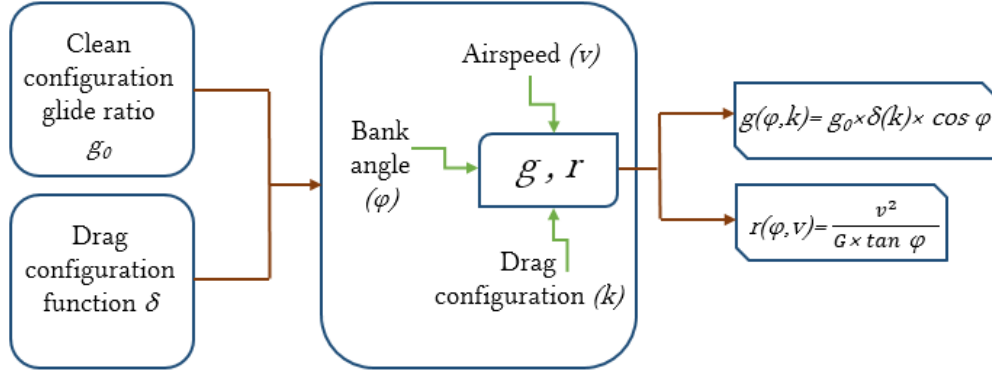


Fig. 2.5: The damaged aircraft model.

the aircraft sensors to estimate the observed glide ratio $\hat{g}(\theta, k)$. This is done by using the pressure altitude (z) and the airspeed (v_x) that are available from the sensor data every second. For a given instant t_i , we can compute the observed glide ratio $\hat{g}(\theta, k)(t_i)$ by taking a ratio of the horizontal distance traveled to the altitude lost in the preceding η seconds (Eq. 2.19).

$$\hat{g}(\theta, k)(t_i) = \frac{\Delta x(\eta)}{\Delta z(\eta)} = \frac{\sum_{i-\eta}^i v_x(t_i)}{z(t_{i-\eta}) - z(t_i)} \quad (2.19)$$

where $\Delta x(\eta)$ is the horizontal distance covered in preceding η seconds and $\Delta z(\eta)$ is the altitude loss in the same interval. In order to ensure that anomalous data is not used for computing the baseline glide ratio, we detect *stable windows of descent* for filtering out such data. A stable window of descent satisfies the following conditions:

- It is a period ω of steady descent with no vertical acceleration.

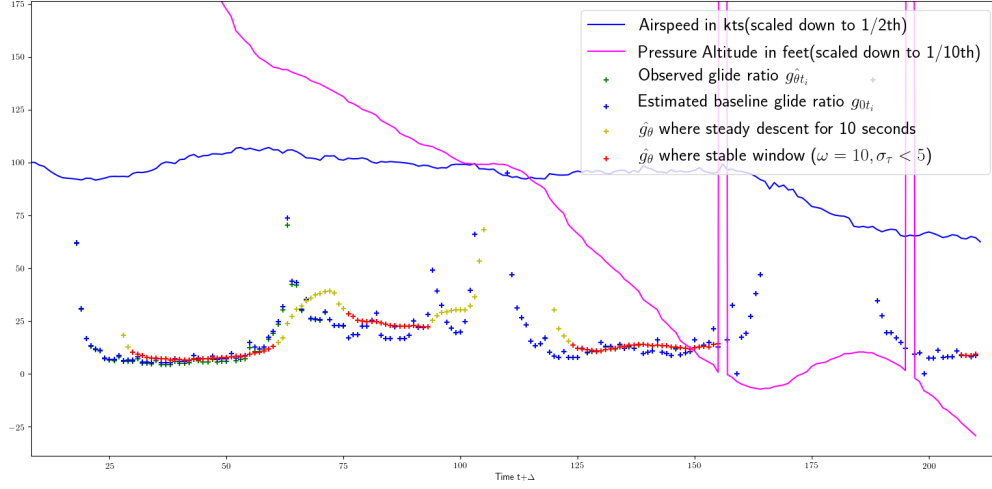


Fig. 2.6: Estimation of glide ratio from sensors (FDR data of US Airways 1549).

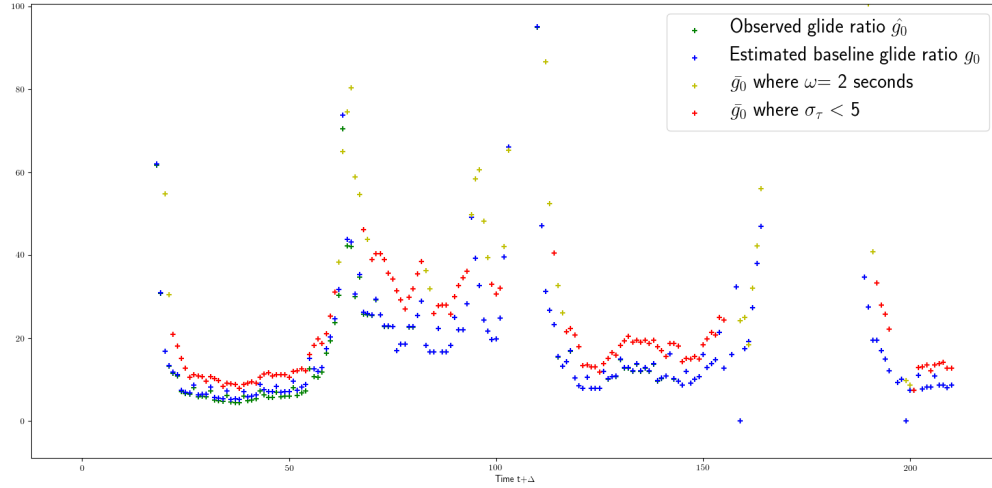


Fig. 2.7: Effect of too short size of ω .

- The distribution of $\hat{g}(\theta, k)(t_i)$ in the period ω has a standard deviation within a threshold σ_τ .

When we detect a stable window of descent ω , we compute the observed glide ratio $\hat{g}(\theta, k)(\omega)$ for the observed bank angle θ by taking a mean of all values of glide ratios observed in ω (Eq. 2.20).

$$\hat{g}(\theta, k)(\omega) = \frac{\sum_{i=1}^n \hat{g}(\theta, k)(t_i)}{n} \text{ for all } t_i \in \omega \quad (2.20)$$

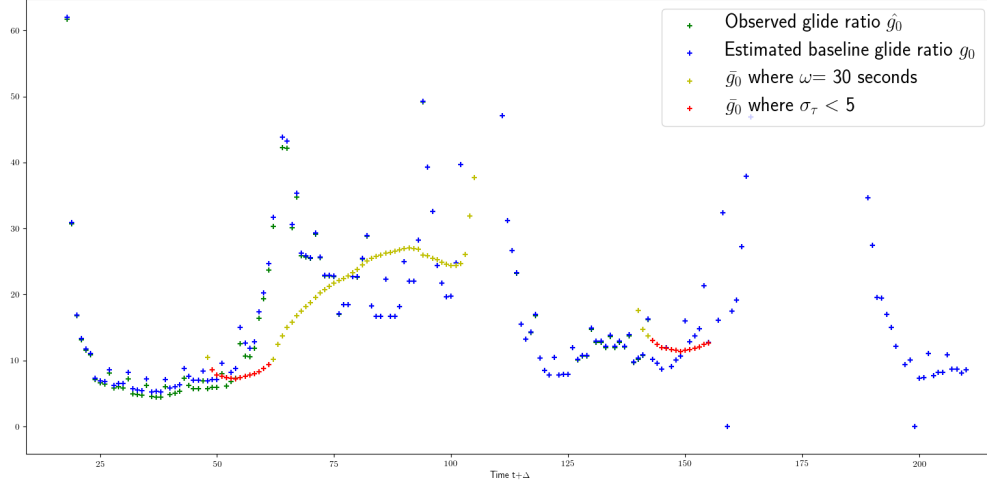


Fig. 2.8: Effect of too large size of ω .

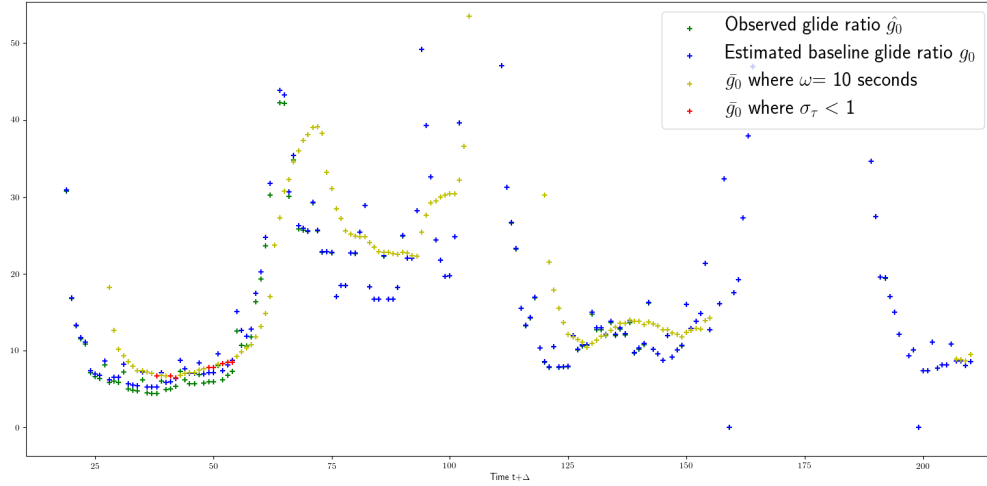


Fig. 2.9: Effect of too small value of σ_τ .

In our experiments, we take $\eta = 4$, ω of duration 10 seconds and $\sigma_\tau = 5$ (Fig. 2.6). The choice of these values have a major impact on the estimation of $\hat{g}(\theta, k)$ because too short or too large values of ω and σ_τ make it difficult to filter out noisy values of \hat{g}_θ (Fig. 2.7 to Fig. 2.10).

The observed glide ratio for airspeed, bank angle and drag configuration are then sent to the model refinement component. The model refinement component calculates the new baseline glide ratio $g_0'(\omega)$ using the observed bank angle θ , drag configuration k from the

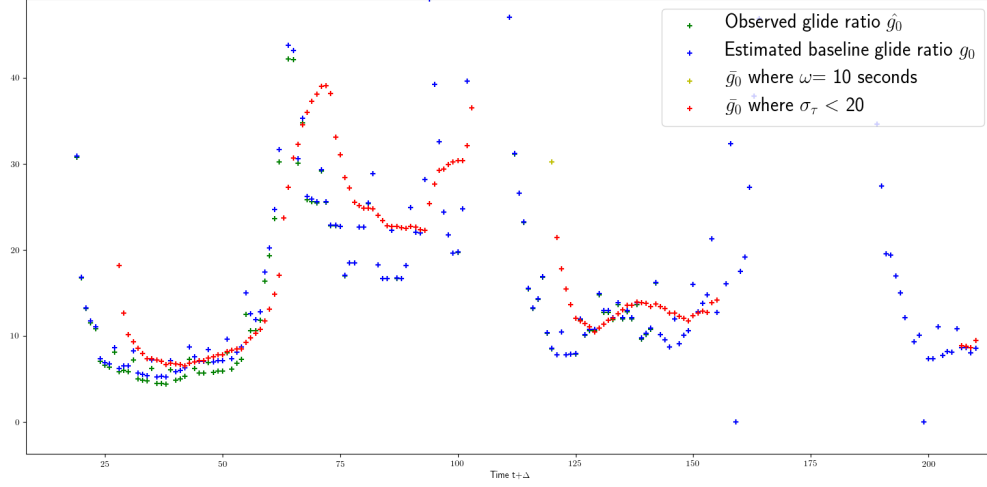
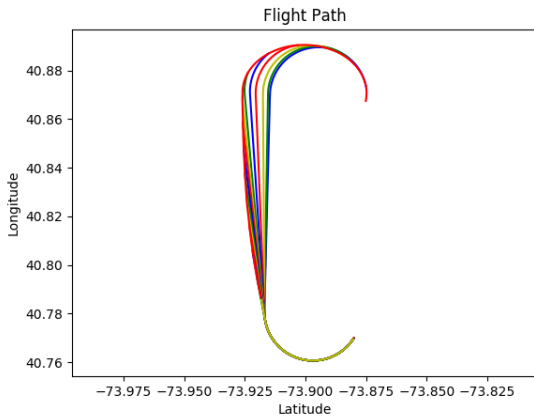


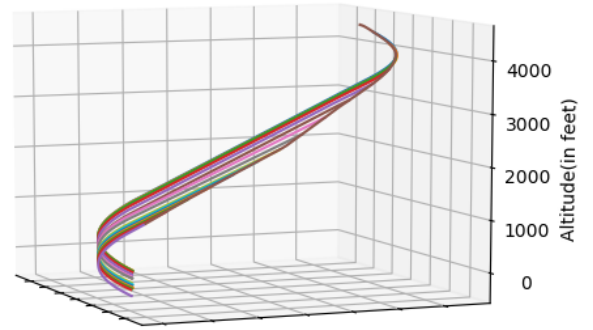
Fig. 2.10: Effect of too large value of σ_τ .

sensor data, and the observed glide ratio $\hat{g}(\theta, k)(\omega)$ (Eq. 2.21). This is done assuming that the aircraft is maintaining the best gliding airspeed for clean configuration.

$$\hat{g}(\theta, k)(\omega) = g_0'(\omega)\delta(k) \cos \theta \implies g_0'(\omega) = \frac{\hat{g}(\theta, k)(\omega)}{\delta(k) \cos \theta} \quad (2.21)$$



(a) 2D View.



(b) 3D View.

Fig. 2.11: Trajectories to LGA4 from an altitude of 4551 feet. New trajectories computed using data from flight simulator.

Fig. 2.11 shows dynamic data driven approach being used to generate trajectories to LGA4 from an altitude of 4451 feet. An initial trajectory was first generated using a

baseline glide ratio of 16:1 and was flown in a flight simulator. During the simulated flight, new baseline glide ratios were computed from the simulator data and new trajectories were generated. The image clearly shows that correcting the baseline glide ratio from flight data can have a major impact on new trajectories that are generated. This allows us to account for dynamic factors such as partial power, wind, and aircraft surface damage and compute a feasible trajectory corresponding to the actual flight capabilities of an aircraft during an emergency.

2.5 Trajectory Planning Algorithm

LOT emergencies can occur at any altitude. Depending on the altitude of the emergency, the nature of possible trajectories varies. Owen *et al.* [7] describe three types of trajectories depending on the altitude of the aircraft with respect to the runway, namely, *low altitude*, *middle altitude* and *high altitude* trajectories. Our trajectory planning algorithm (Fig. 2.12) introduces the concept of an *extended runway segment* to classify emergencies into only two scenarios: *low altitude scenarios* and *high altitude scenarios*.

A low altitude scenario is an emergency altitude from which a simple Dubins airplane path can bring the aircraft down to the runway or above the runway at an altitude from where integral number of spiral turns are not possible. In this case, the generated trajectory consists of a simple Dubins 3D airplane path from the starting point to the runway (Fig. 2.13).

A high altitude scenario is any emergency altitude from which a simple Dubins airplane path brings an aircraft over the runway at an altitude from where integral number of spiral turns are possible. In certain situations, just spiral turns may not be enough to lose the excess altitude in its entirety and in such cases our algorithm generates an *extended runway segment* in addition to spiral turns (Fig. 2.13). This extended runway segment has a length e , such that $e \in [0, 2\pi r(\theta, v_x)g(0, d)/g(\theta, c))$, where $g(0, d)$ is the *dirty configuration glide ratio* for straight line gliding and $g(\theta, c)$ is the clean configuration glide ratio for banked turns. The addition of this extended runway segment in the final path allows the aircraft to lose the excess altitude before reaching the runway.

We use a dirty configuration glide ratio in the extended final segments. This ensures that the starting point of the extended final segment is at an altitude h_d from which the flight can safely make it to the runway (Fig. 2.14). In case the aircraft reaches the starting point of the final segment at an altitude $h_a > h_d$, then the pilot will have the flexibility of

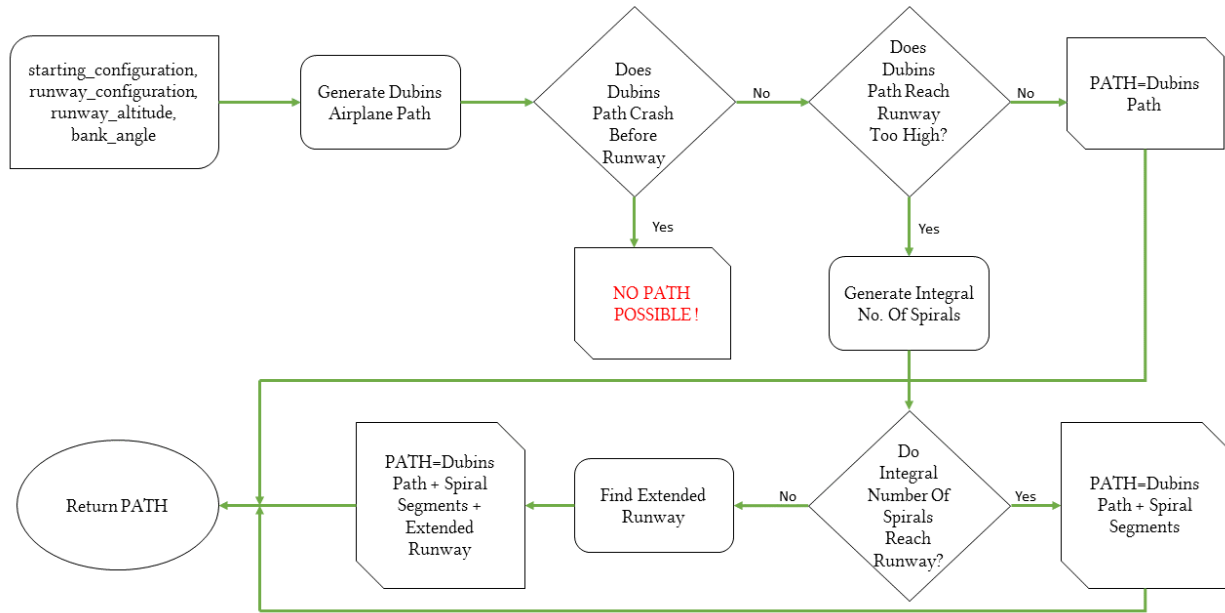


Fig. 2.12: Flowchart of trajectory planning algorithm.

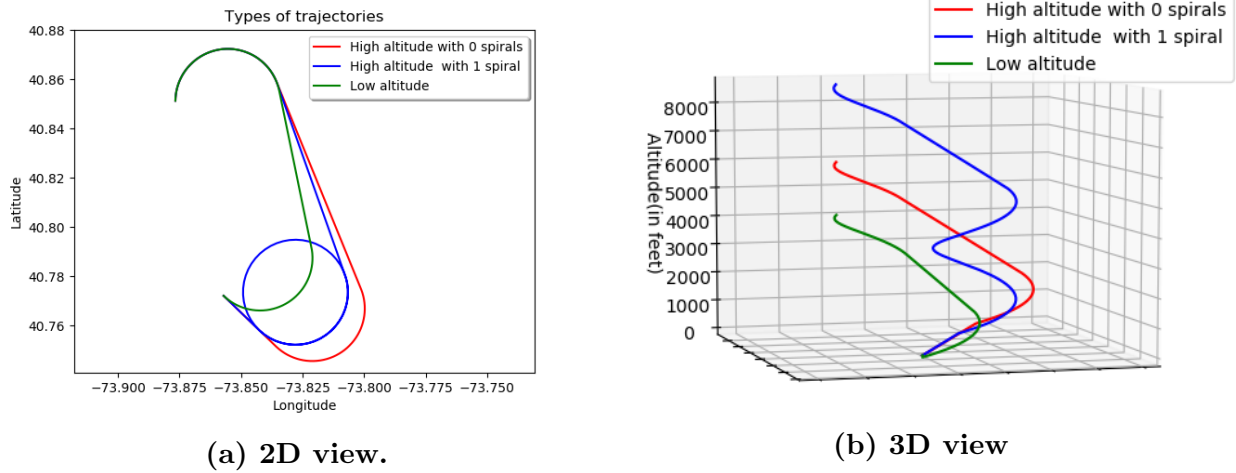
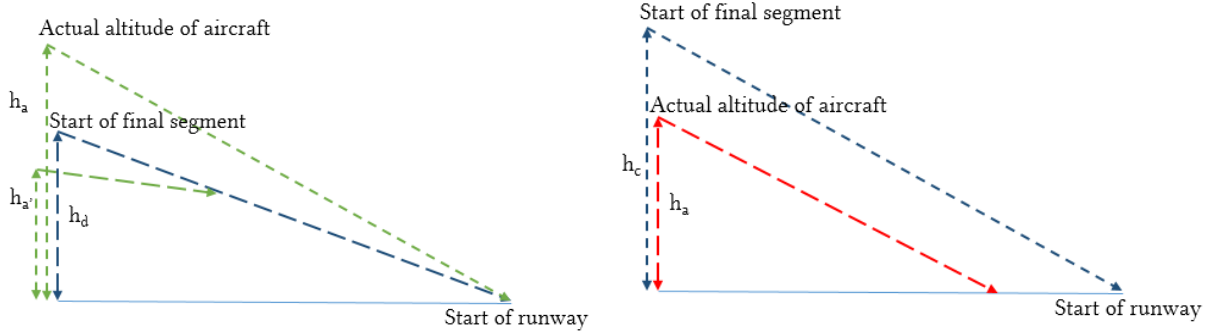


Fig. 2.13: Low and high altitude trajectories with extended runway segments.

losing the excess altitude $h_a - h_d$ by increasing drag or by adjusting side-slip and forward slip, and still making it to the runway (Fig. 2.14a). On the other hand, if the aircraft reaches the starting point of the final segment at an altitude $h_{a'} < h_d$, then the pilot can keep using clean configuration until it is safe to increase drag and make a successful landing (Fig. 2.14a). However, if a clean configuration glide ratio is used for computing the final segment, then it will start at an altitude h_c that is too optimistic. In case the aircraft reaches the start of

the final segment at an altitude $h_a < h_c$, it will be impossible to reach the runway from that position (Fig. 2.14b).



(a) Using a dirty configuration glide ratio. (b) Using a clean configuration glide ratio.

Fig. 2.14: Significance of using a dirty configuration glide ratio in the final segment.

Our trajectory generation algorithm generates trajectories that consist of a series of standard maneuvers (constant-bank turns and straight line glide). However, it should be noted that our current algorithm fails to return trajectories in certain cases, for example, when the aircraft is directly above the runway. It can generate trajectories *only* for those cases where the Dubins airplane path from initial to final configurations consists of a curve, followed by a straight line segment, followed by a curve.

2.6 Trajectory Safety Metrics

We introduce a set of *trajectory safety metrics* to evaluate our trajectories. Each trajectory \mathbb{T} generates a value for each metric and each of these values are then normalized relative to the minimum ($\|m\| = \frac{m_{min}}{m}$) or maximum ($\|m\| = \frac{m}{m_{max}}$) value, whichever is desired for that metric. The safety metrics that have been considered for this paper are:

- *Average Altitude* (\bar{z})- This metric computes the average of the altitude (z) for all N points in \mathbb{T} . This metric is normalized against the maximum value because for a given trajectory, a higher average altitude from the ground is desirable (Eq. 2.22).

$$\bar{z} = \frac{\sum_{i=0}^N z_i}{N} \quad (2.22)$$

- *Average Distance From Runway* (\bar{d})- This metric computes the average of the distance

(d) from the runway for all N points in \mathbb{T} . This metric is normalized against the minimum value because for a given trajectory, minimum distance from the runway at all time is desirable.

$$\bar{d} = \frac{\sum_{i=0}^N d(r_i, r_R)}{N} \quad (2.23)$$

Eq. 2.23 is used to compute \bar{d} where r_R is the position vector of the runway and $d(r_1, r_2)$ is the distance between r_1 and r_2 in 3D space.

- *Average Bank Angle Over Height ($\frac{\bar{\theta}}{z}$)*- This metric is computed by taking an average of the ratio between bank angle (θ) and altitude (z) for all N points in \mathbb{T} . Since it is not desirable to have steep turns very close to the ground, this metric is normalized against the minimum value (Eq. 2.24).

$$\left(\frac{\bar{\theta}}{z}\right) = \frac{\sum_{i=0}^N \left(\frac{\theta_i}{z_i}\right)}{N} \quad (2.24)$$

- *Total time (t)*- This metric measures the total time required to fly the trajectory \mathbb{T} . It is normalized against the maximum as a trajectory that takes longer time gives the pilots more time to plan a safe landing (Eq. 2.25).

$$t = \frac{\sum_{i=1}^N d(r_i, r_{i-1})}{v_x} \quad (2.25)$$

- *Extended runway segment length (e)*- This metric measures the length (e) of the extended runway segment. Trajectories with longer final straight line approaches are desirable as a longer final approach allows for the pilot to make adjustments to drag and speed easily just before landing. Thus, this metric is normalized against the maximum value. Given the position vector of the starting point of the extended runway segment r_e and the position vector of the runway r_R , we can calculate this metric using Eq. 2.26.

$$e = d(r_e, r_R) \quad (2.26)$$

- *Number of turns (n_T)*- This metric counts the number of turns (n_T) in \mathbb{T} . It is desirable to have as minimum number of turns as possible, hence it is normalized against the

minimum value.

$$n_T = n_{T_D} + n_{T_S} \quad (2.27)$$

Eq. 2.27 can be used to compute n_T where n_{T_D} is the number of left and right turns in the Dubins airplane path and n_{T_S} is the number of 360 degree turns in the spiral segment.

We introduce an *utility function* (u), which is computed by taking the weighted average of the normalized values of the metrics, and is used to rank the trajectories. The rank of a trajectory is directly proportional to the value of its utility function which is given by Eq. 2.28.

$$u = \frac{\sum w_i \|m_i\|}{\sum w_i} \quad (2.28)$$

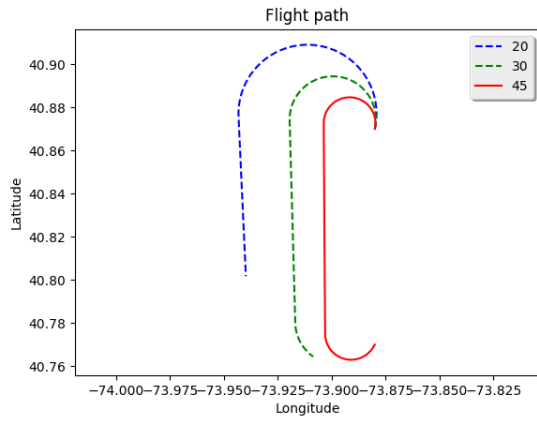
where w_i and $\|m_i\|$ are the weight and normalized value respectively of metric i . This utility function can be easily modified to account for other safety factors like wind, terrain; *etc* in future work.

2.7 Experimentation and Results

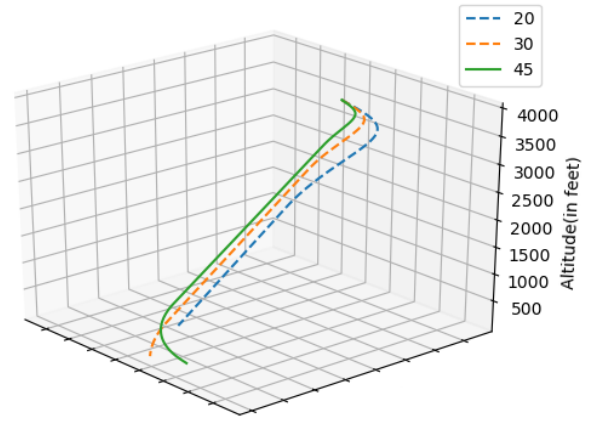
2.7.1 Simulations With La Guardia Airport

We ran simulations with hypothetical scenarios for LGA4, LGA13 and LGA31 of La Guardia airport, New York City. Simulations were done for altitudes of 4000, 6000, 8000 and 10000 feet from the initial configuration: {latitude: 40.86500°, longitude: -73.88000°, heading: 12.9°} (figures 2.15 - 2.26). In all cases, a clean configuration glide ratio of 17.25:1 (as predicted in [8] for an Airbus A320) was used for generating the trajectories, with a dirty configuration glide ratio of 9:1 in the extended final segments.

Fig. 2.15 clearly shows how bank angle can be the determining factor for a feasible trajectory from a given initial configuration. 20° and 30° bank angles took the aircraft away from the runway, causing the aircraft to hit the ground before reaching the runway, while a 45° bank angle kept the aircraft closer to the runway, allowing a flyable trajectory. In all cases, smaller bank angles were more successful in generating feasible trajectories. Again, Fig. 2.16 and Fig. 2.26 show that in certain scenarios, for the same initial and final configurations, the nature of the initial 3D Dubin's path may be different for different bank angles.

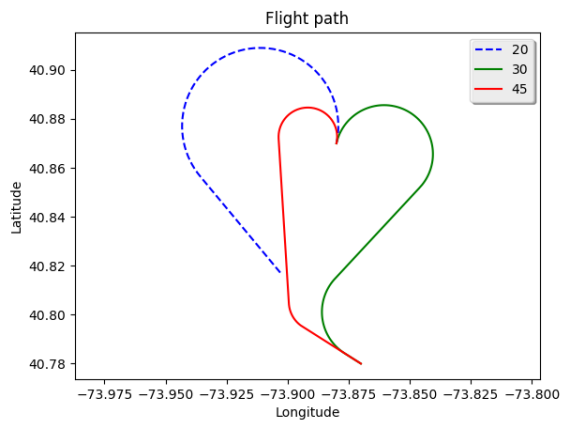


(a) 2D View.

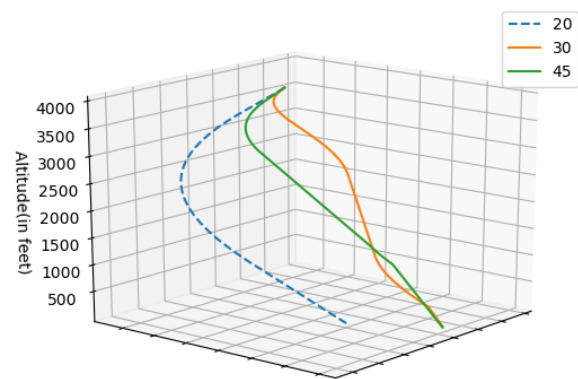


(b) 3D View.

Fig. 2.15: Trajectory to LGA4 from 4000 feet.

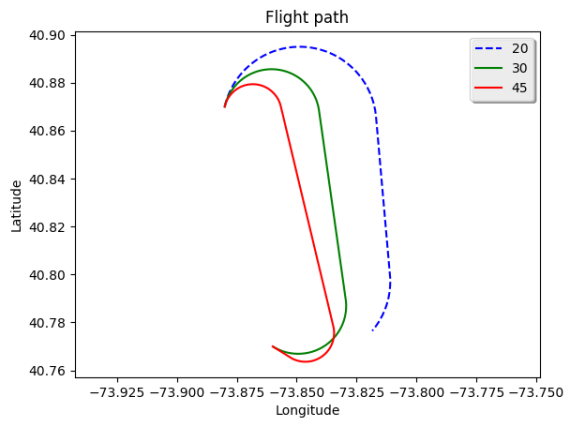


(a) 2D View.

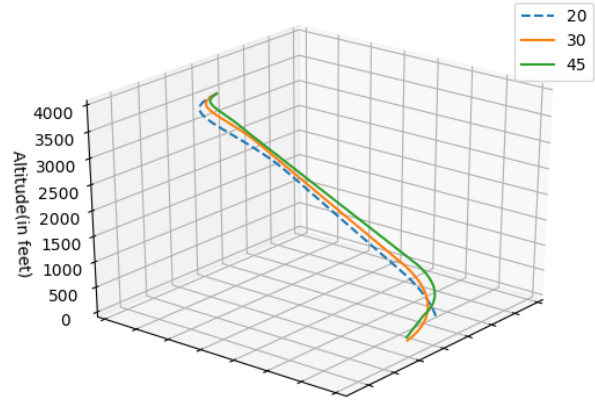


(b) 3D View.

Fig. 2.16: Trajectory to LGA13 from 4000 feet.

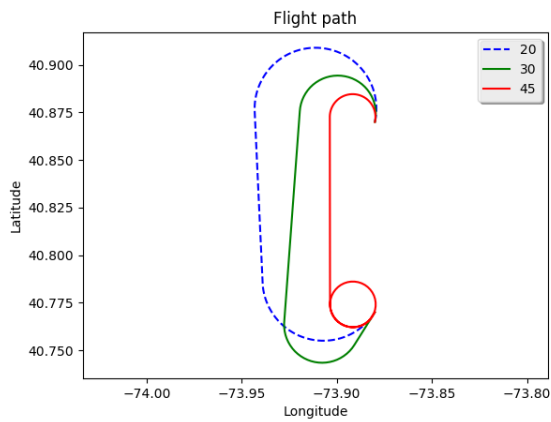


(a) 2D View.

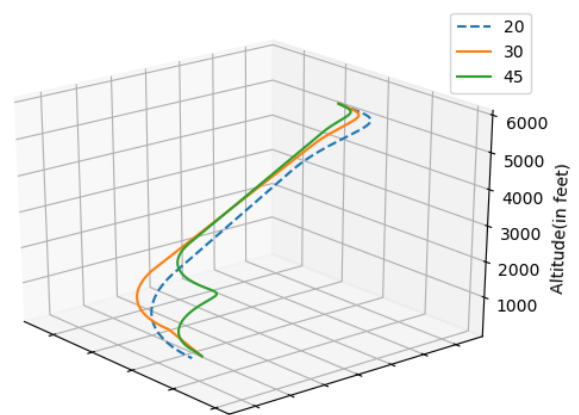


(b) 3D View.

Fig. 2.17: Trajectory to LGA31 from 4000 feet.

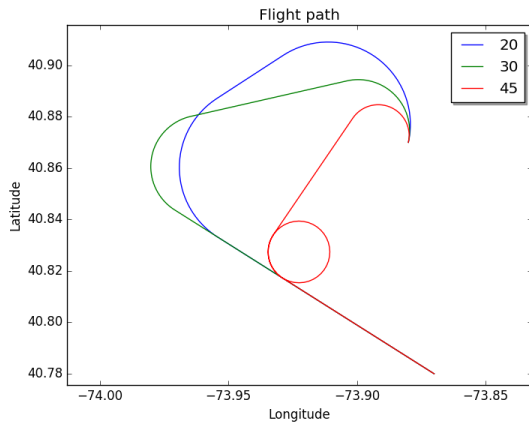


(a) 2D View.

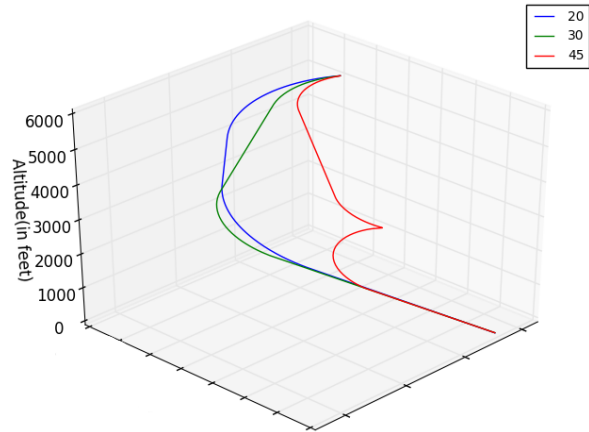


(b) 3D View.

Fig. 2.18: Trajectory to LGA4 from 6000 feet.

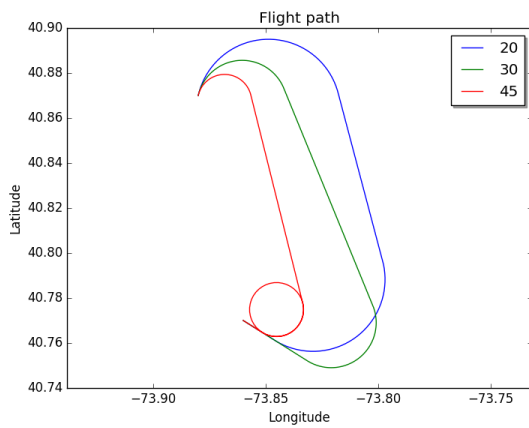


(a) 2D View.

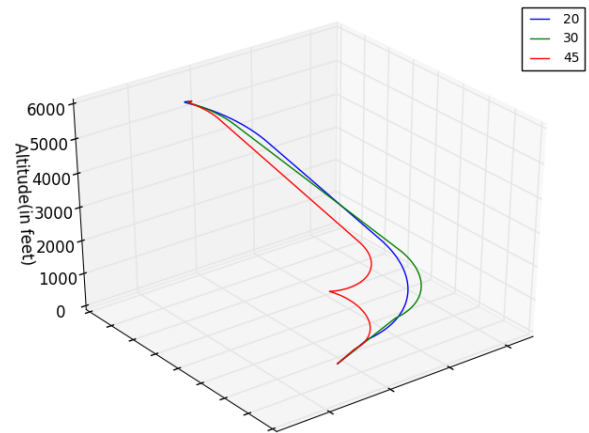


(b) 3D View.

Fig. 2.19: Trajectory to LGA13 from 6000 feet.

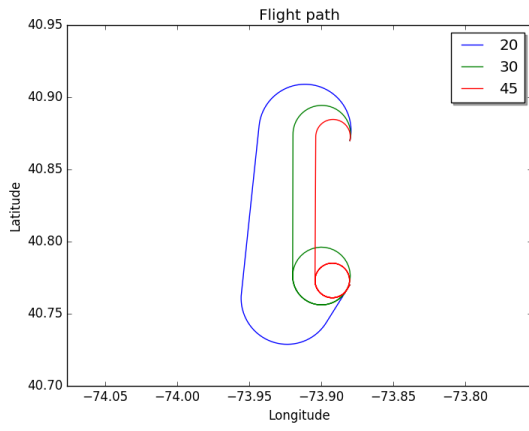


(a) 2D View.

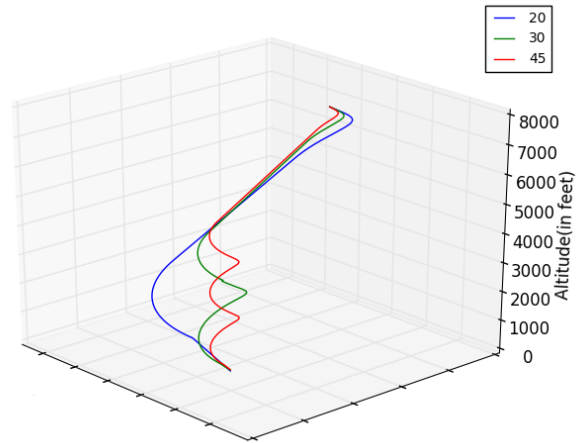


(b) 3D View.

Fig. 2.20: Trajectory to LGA31 from 6000 feet.

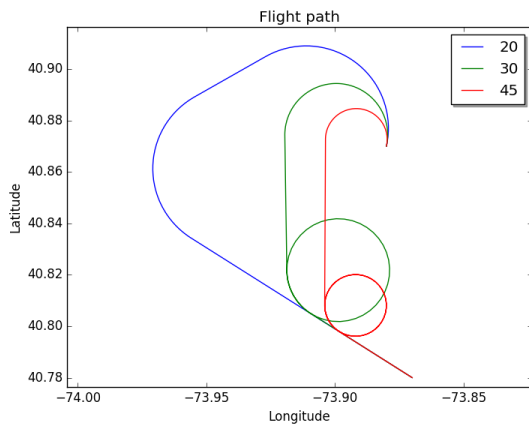


(a) 2D View.

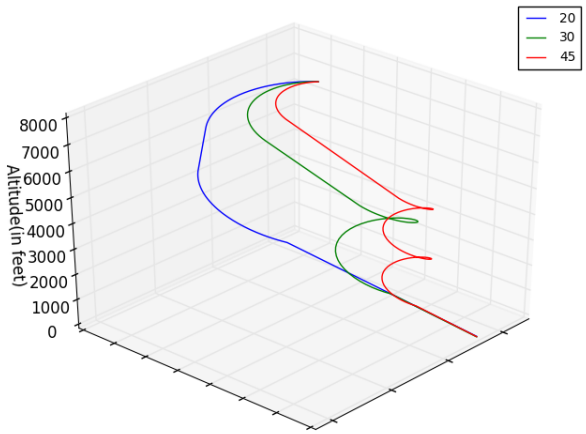


(b) 3D View.

Fig. 2.21: Trajectory to LGA4 from 8000 feet.

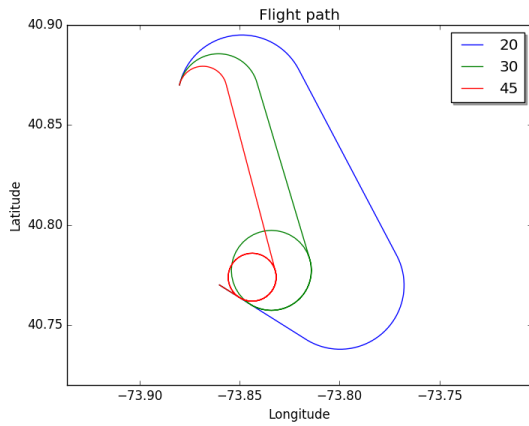


(a) 2D View.

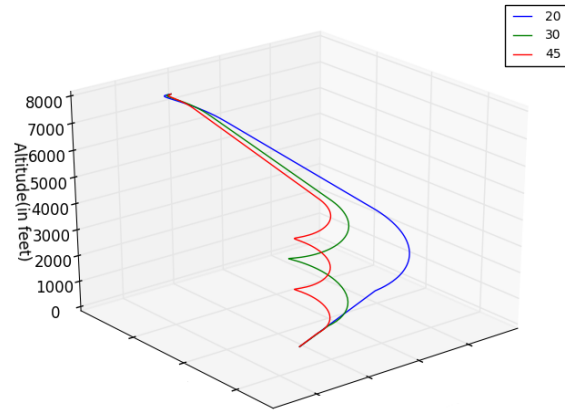


(b) 3D View.

Fig. 2.22: Trajectory to LGA13 from 8000 feet.

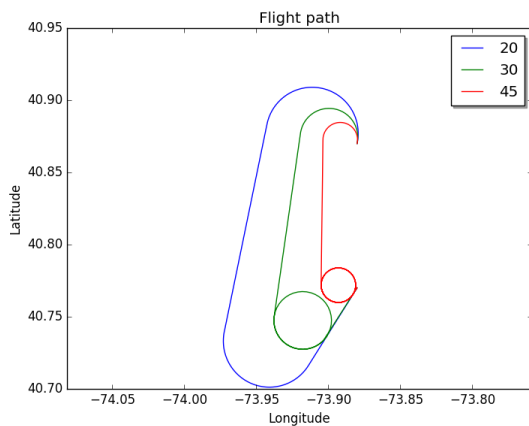


(a) 2D View.

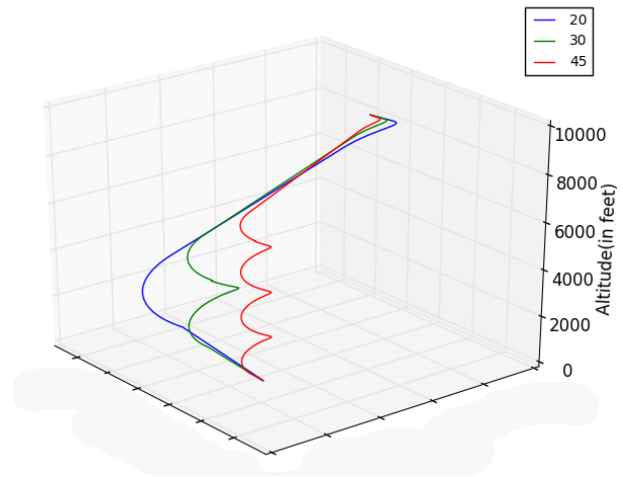


(b) 3D View.

Fig. 2.23: Trajectory to LGA31 from 8000 feet.

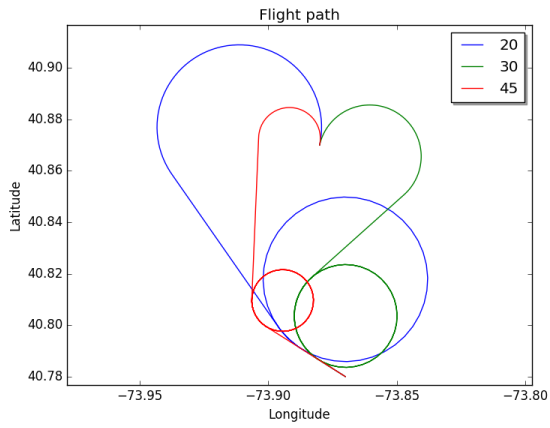


(a) 2D View.

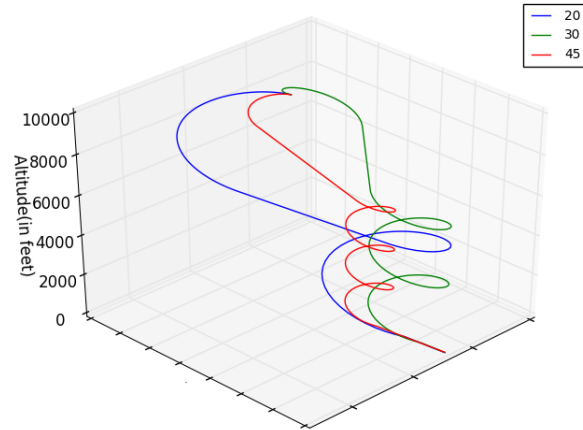


(b) 3D View.

Fig. 2.24: Trajectory to LGA4 from 10000 feet.

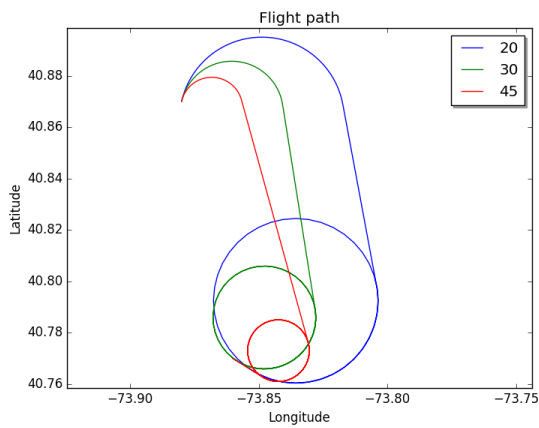


(a) 2D View.

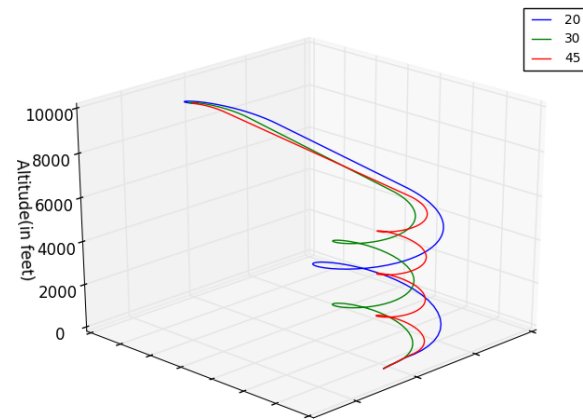


(b) 3D View.

Fig. 2.25: Trajectory to LGA13 from 10000 feet.



(a) 2D View.



(b) 3D View.

Fig. 2.26: Trajectory to LGA31 from 10000 feet.

2.7.2 Analysis of Alternate Landing Options for US Airways Flight 1549

US Airways flight 1549 took off from New York City’s La Guardia airport on January 15, 2009 and lost power in both engines when it struck a flock of Canada geese a couple of minutes after takeoff. The pilots managed to land the Airbus A320-214 successfully in the Hudson river and save the lives of everyone on board the aircraft. We considered the incident of flight 1549 as a test case to evaluate the effectiveness of our trajectory generation algorithm. We collected the Flight Data Recorder data as published by the National Transportation Safety Board (NTSB) (Table 2.3) and simulated scenarios from $t + 4$ through $t + 40$ seconds (t being the time when the pilot said "birds" (15:27:10 UTC), as determined from the sound recording in the Flight Data Recorder). From the data (Fig. 2.27), it is clearly visible that the flight kept gaining altitude until $t + 16$ seconds and attained a maximum altitude of 3352 feet before finally beginning to descend. Since the GPS data was only available at 4 second intervals, we ran our algorithm at 4 second intervals. We used two values of clean configuration glide ratios: 17.25:1, as predicted by [8], and 19:1, as shown by our simulator. A dirty configuration glide ratio of 9:1 was used for the final extended runway approaches in both cases.

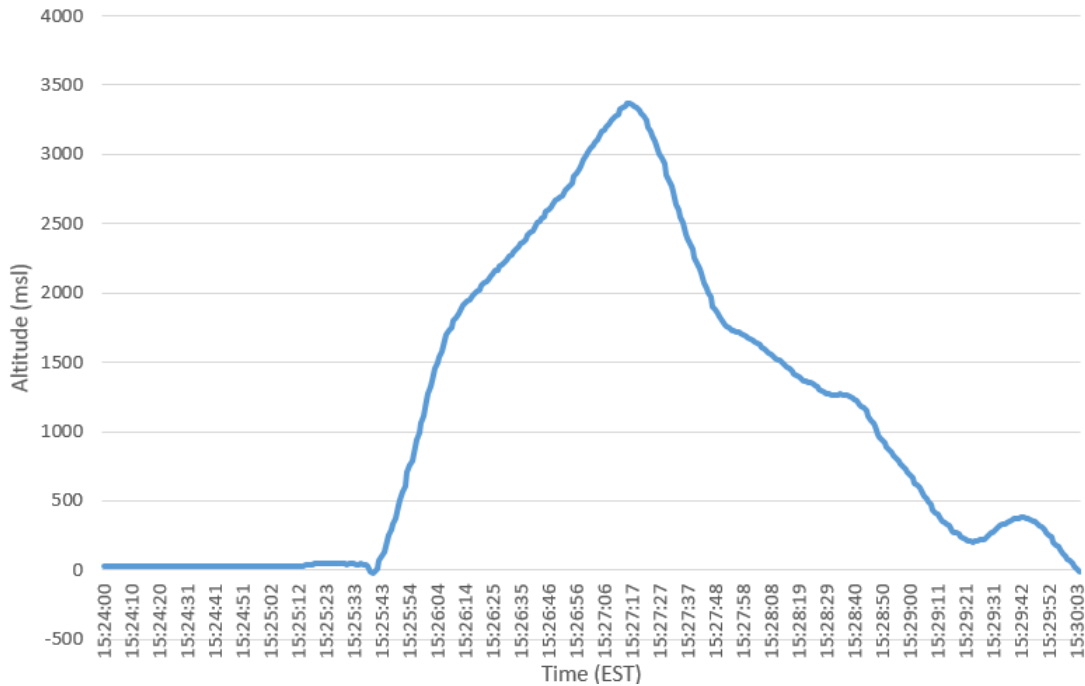
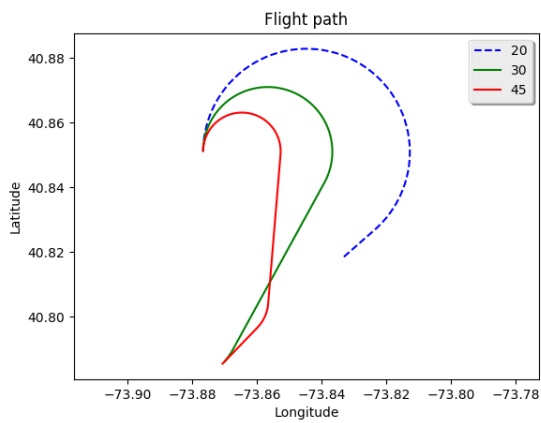


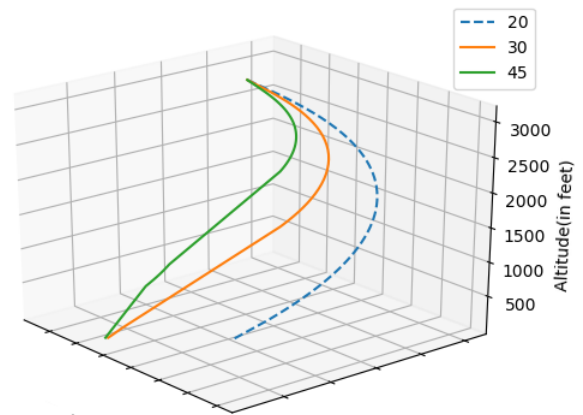
Fig. 2.27: Flight 1549 Time vs Altitude graph.

Table 2.3: US Airways 1549 relevant Flight Data Recorder data.

Time	Latitude (decimal)	Longitude (decimal)	Pressure Altitude (feet)	True Altitude (feet)	Magnetic Heading (degrees)	Airspeed (kts)
t	40.8477	-73.8758	2792	3056	0	218
t+4	40.8513	-73.8767	2888	3152	0.7	207.125
t+8	40.8547	-73.8781	2968	3232	0	200.25
t+12	40.8581	-73.8786	3048	3312	0.4	193
t+16	40.8617	-73.8794	3088	3352	358.9	185.25
t+20	40.865	-73.88	3040	3304	357.2	185.25
t+24	40.8678	-73.8806	2916	3180	352.6	185.375
t+28	40.8711	-73.8819	2760	3024	344.5	187
t+32	40.8739	-73.8842	2580	2844	333.3	190.625
t+36	40.761	-73.8861	2368	2632	320.6	198.75
t+40	40.8789	-73.8897	2156	2420	305.5	202.875

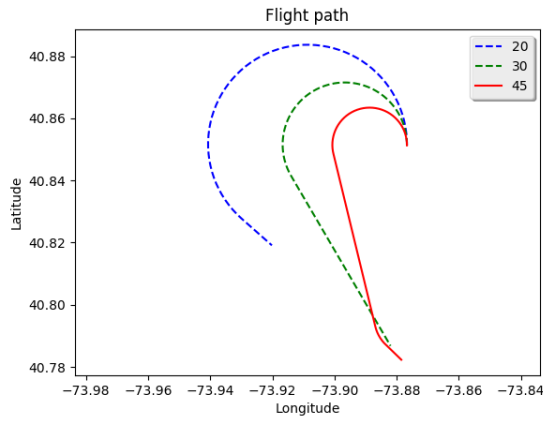


(a) 2D View.

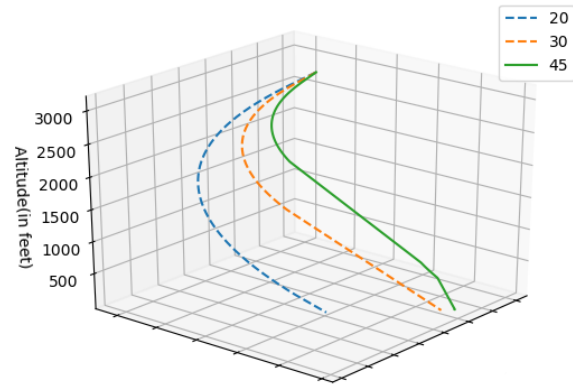


(b) 3D View.

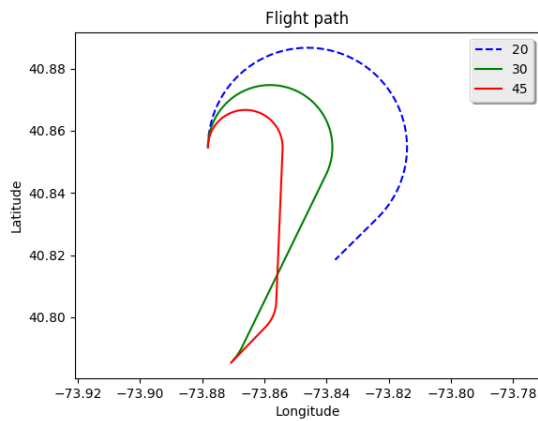
Fig. 2.28: Trajectory to LGA22 with a glide ratio of 17.25:1 at time t+4 .



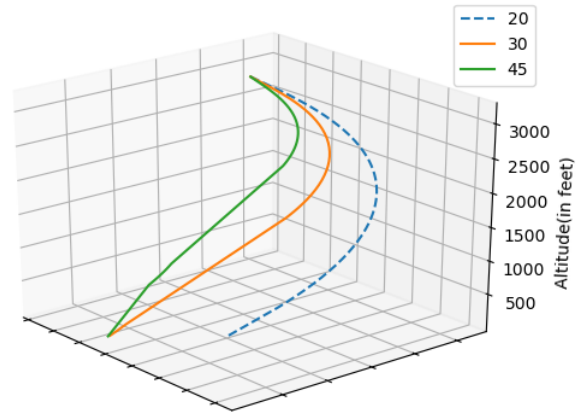
(a) 2D View.



(b) 3D View.

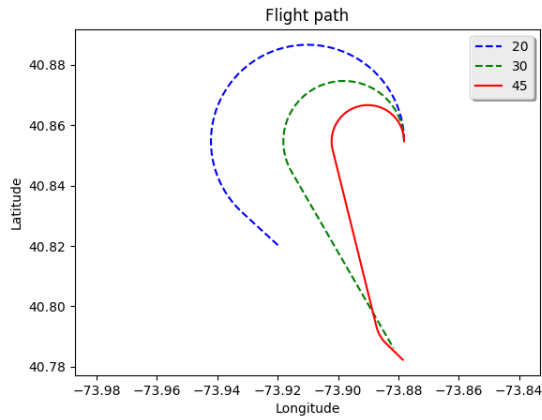
Fig. 2.29: Trajectory to LGA13 with a glide ratio of 17.25:1 at time $t+4$.

(a) 2D View.

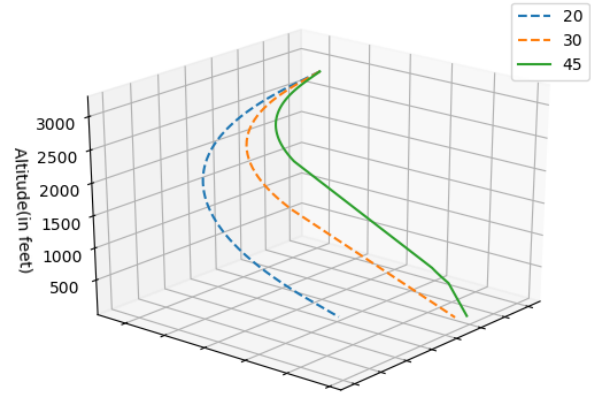


(b) 3D View.

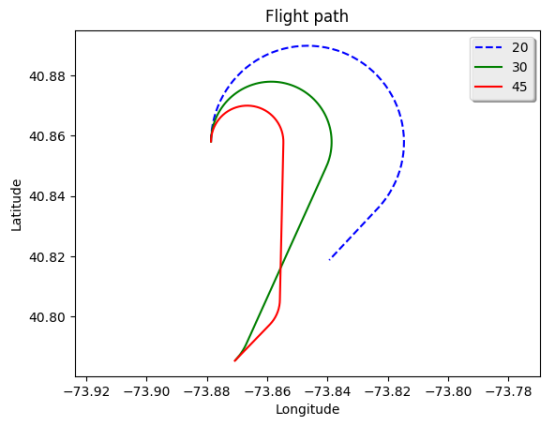
Fig. 2.30: Trajectory to LGA22 with a glide ratio of 17.25:1 at time $t+8$.



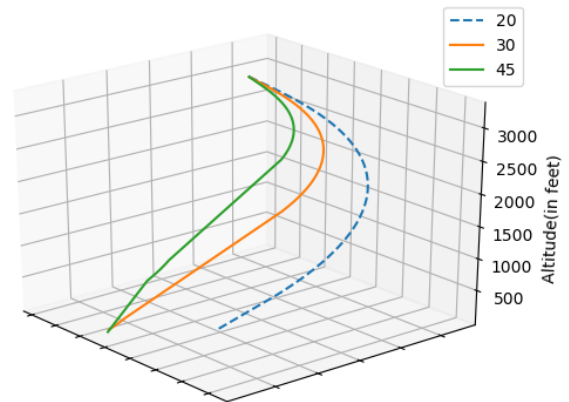
(a) 2D View.



(b) 3D View.

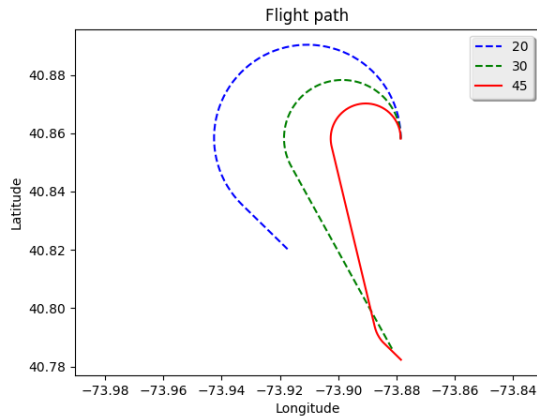
Fig. 2.31: Trajectory to LGA13 with a glide ratio of 17.25:1 at time $t+8$.

(a) 2D View.

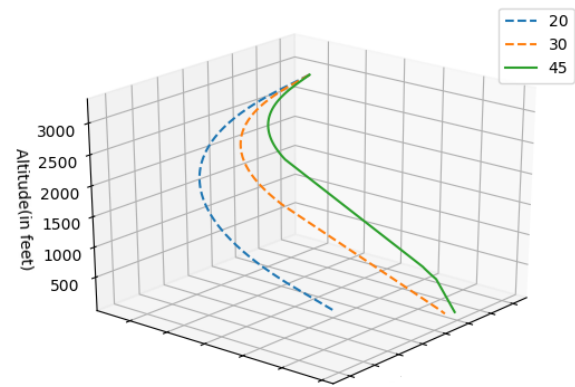


(b) 3D View.

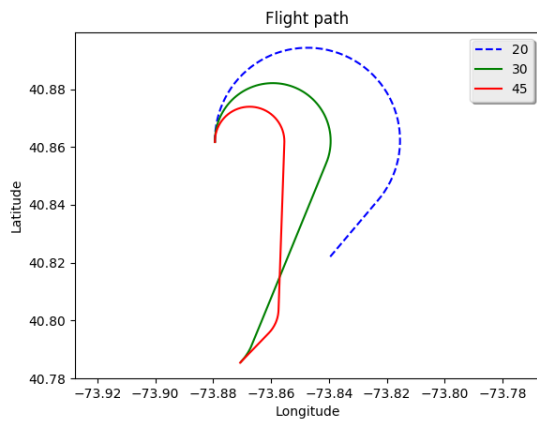
Fig. 2.32: Trajectory to LGA22 with a glide ratio of 17.25:1 at time $t+12$.



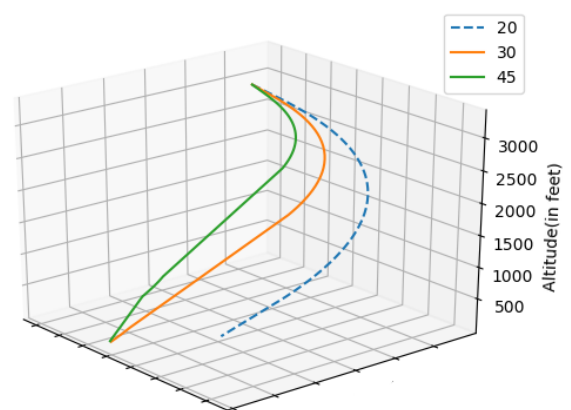
(a) 2D View.



(b) 3D View.

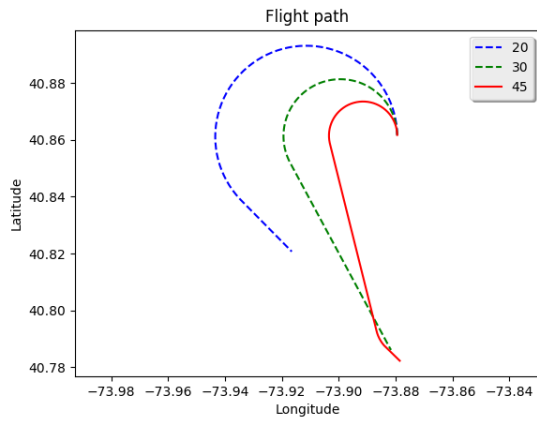
Fig. 2.33: Trajectory to LGA13 with a glide ratio of 17.25:1 at time $t+12$.

(a) 2D View.

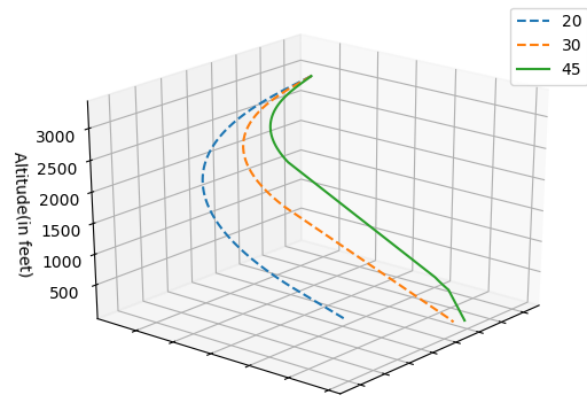


(b) 3D View.

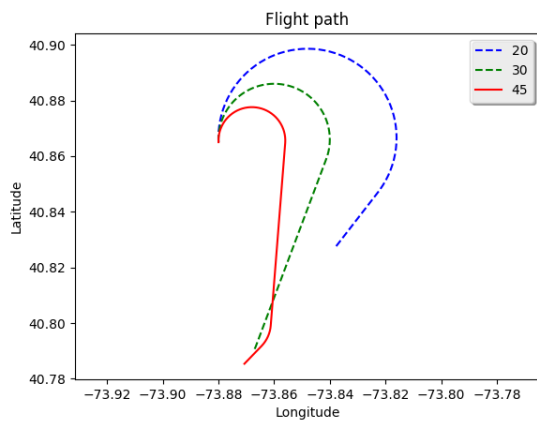
Fig. 2.34: Trajectory to LGA22 with a glide ratio of 17.25:1 at time $t+16$.



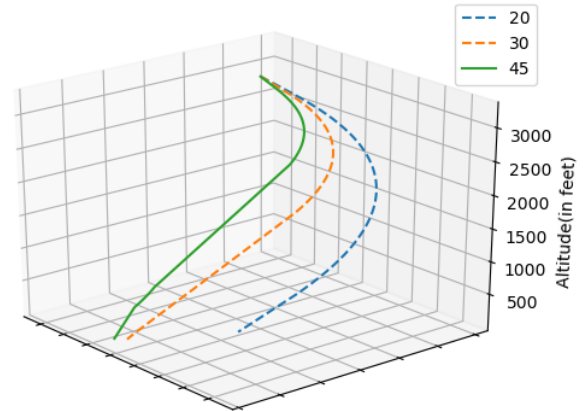
(a) 2D View.



(b) 3D View.

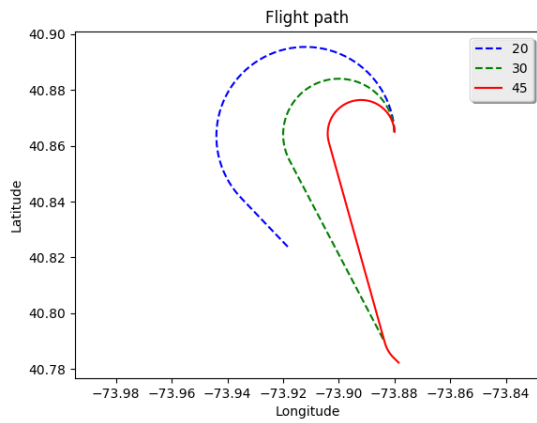
Fig. 2.35: Trajectory to LGA13 with a glide ratio of 17.25:1 at time $t+16$.

(a) 2D View.

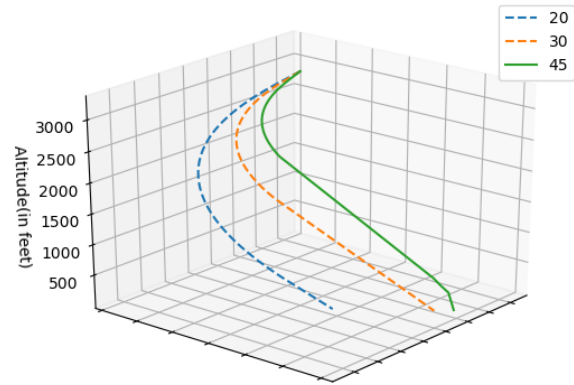


(b) 3D View.

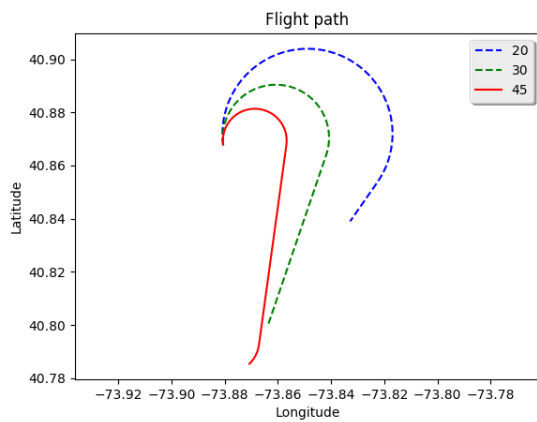
Fig. 2.36: Trajectory to LGA22 with a glide ratio of 17.25:1 at time $t+20$.



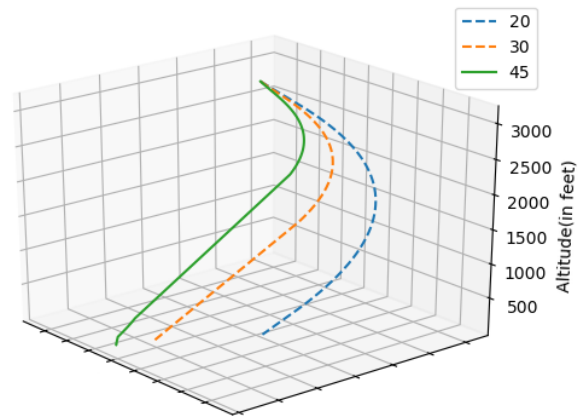
(a) 2D View.



(b) 3D View.

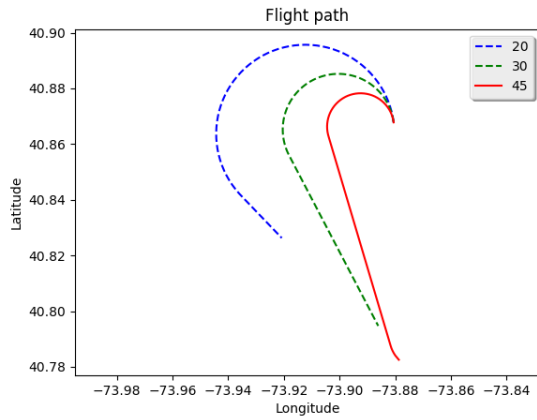
Fig. 2.37: Trajectory to LGA13 with a glide ratio of 17.25:1 at time $t+20$.

(a) 2D View.

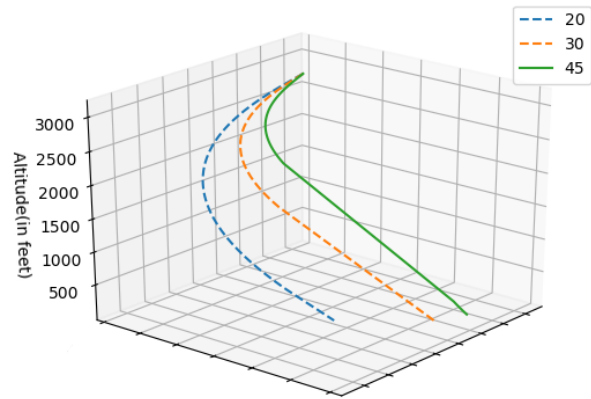


(b) 3D View.

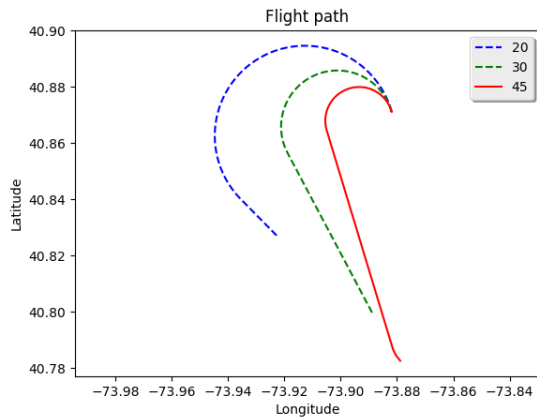
Fig. 2.38: Trajectory to LGA22 with a glide ratio of 17.25:1 at time $t+24$.



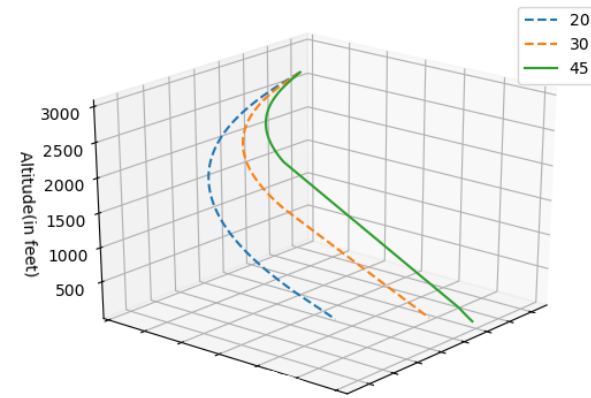
(a) 2D View.



(b) 3D View.

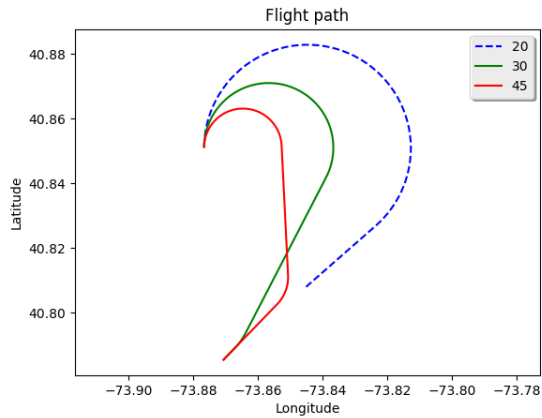
Fig. 2.39: Trajectory to LGA13 with a glide ratio of 17.25:1 at time $t+24$.

(a) 2D View.

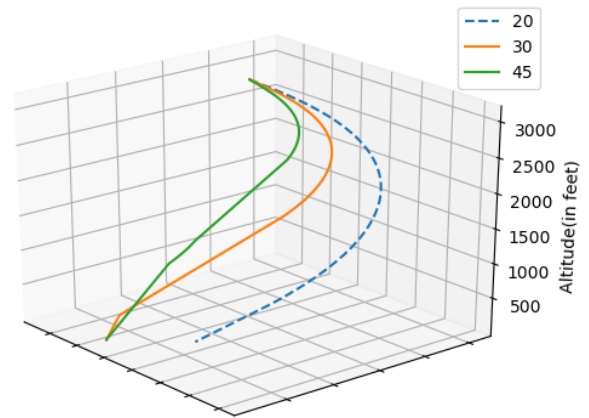


(b) 3D View.

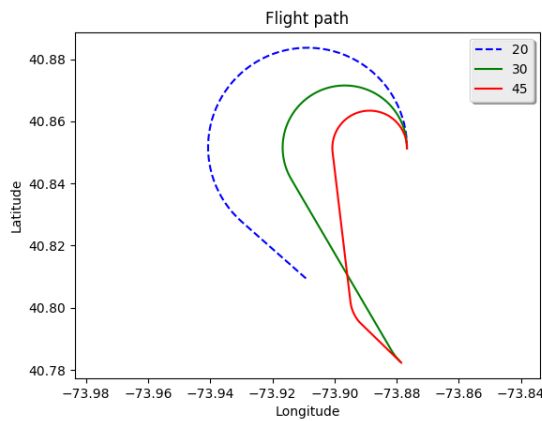
Fig. 2.40: Trajectory to LGA13 with a glide ratio of 17.25:1 at time $t+28$.



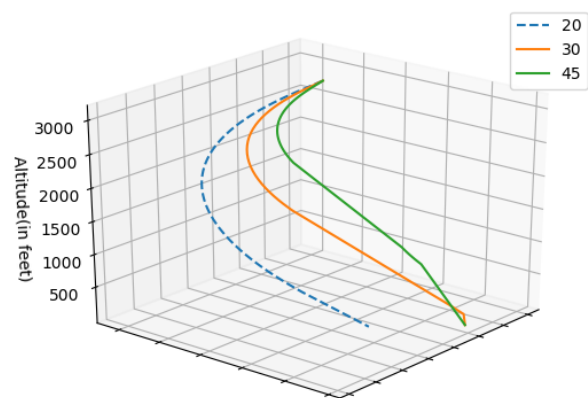
(a) 2D View.



(b) 3D View.

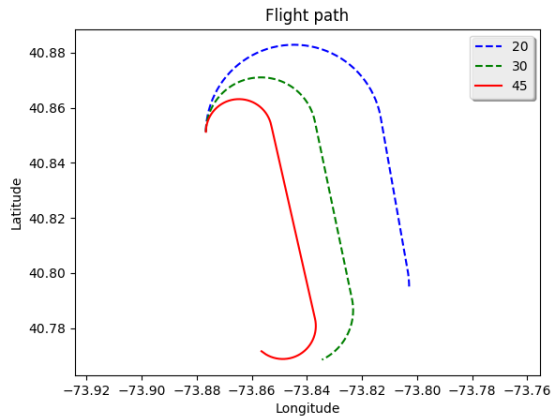
Fig. 2.41: Trajectory to LGA22 with a glide ratio of 19:1 at time $t+4$.

(a) 2D View.

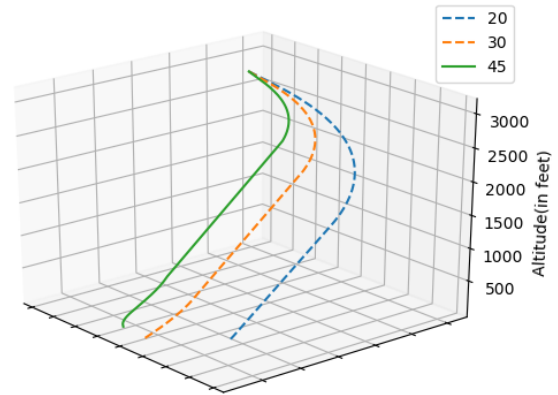


(b) 3D View.

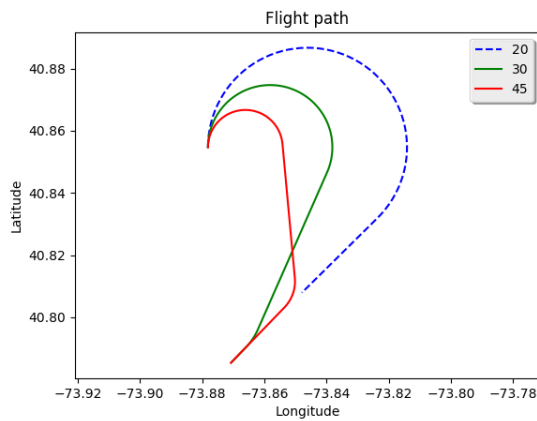
Fig. 2.42: Trajectory to LGA13 with a glide ratio of 19:1 at time $t+4$.



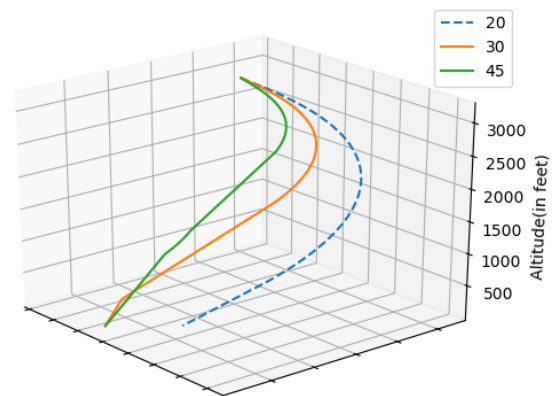
(a) 2D View.



(b) 3D View.

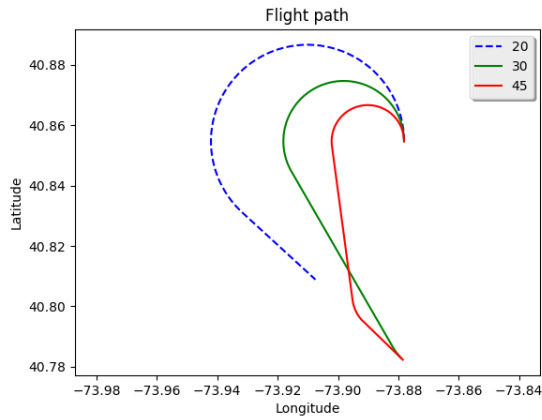
Fig. 2.43: Trajectory to LGA31 with a glide ratio of 19:1 at time $t+4$.

(a) 2D View.

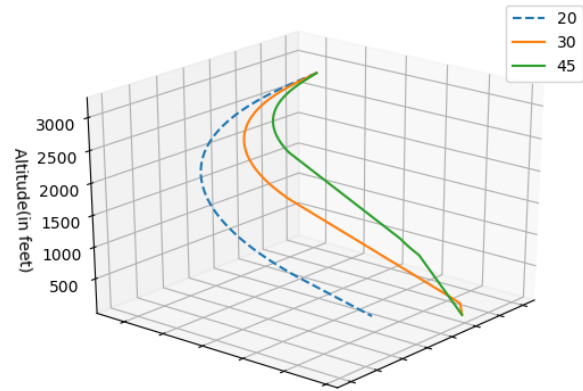


(b) 3D View.

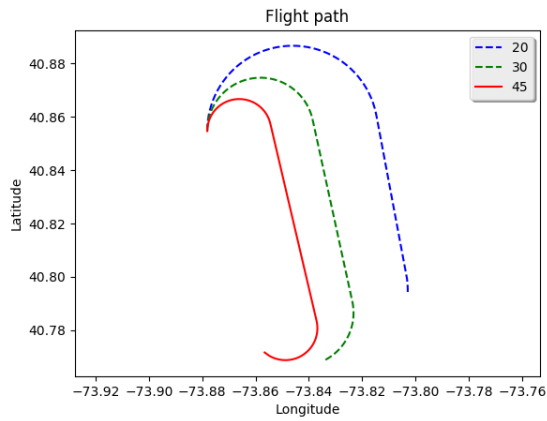
Fig. 2.44: Trajectory to LGA22 with a glide ratio of 19:1 at time $t+8$.



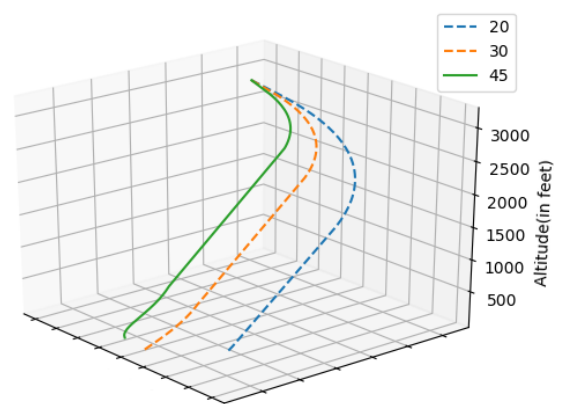
(a) 2D View.



(b) 3D View.

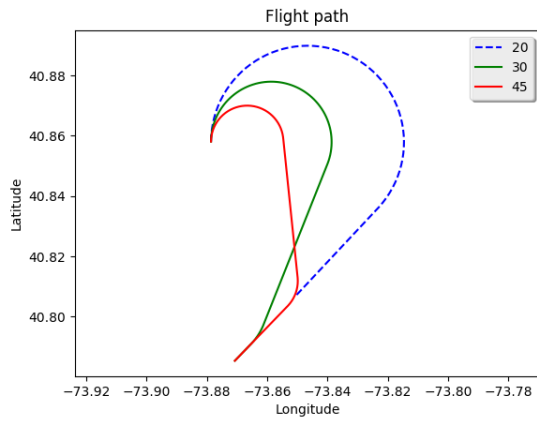
Fig. 2.45: Trajectory to LGA13 with a glide ratio of 19:1 at time $t+8$.

(a) 2D View.

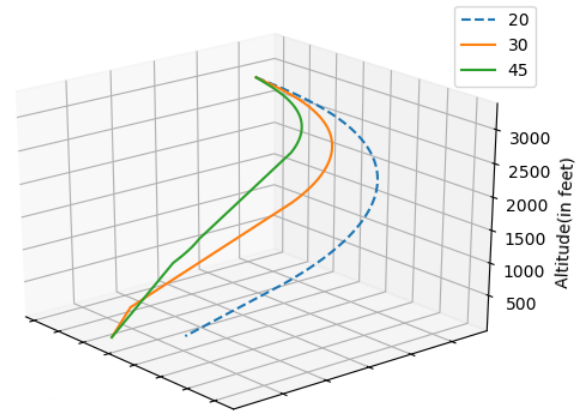


(b) 3D View.

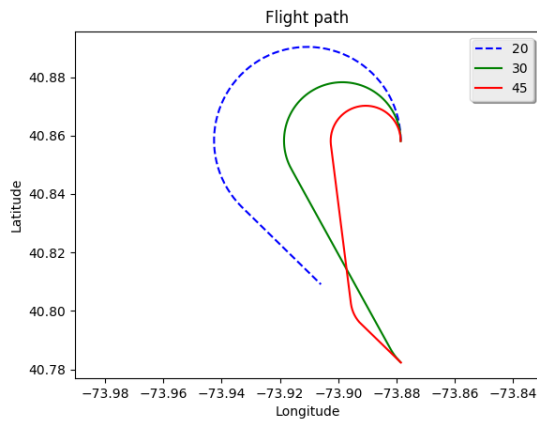
Fig. 2.46: Trajectory to LGA31 with a glide ratio of 19:1 at time $t+8$.



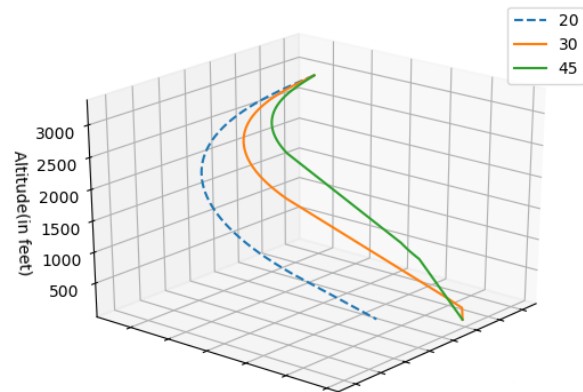
(a) 2D View.



(b) 3D View.

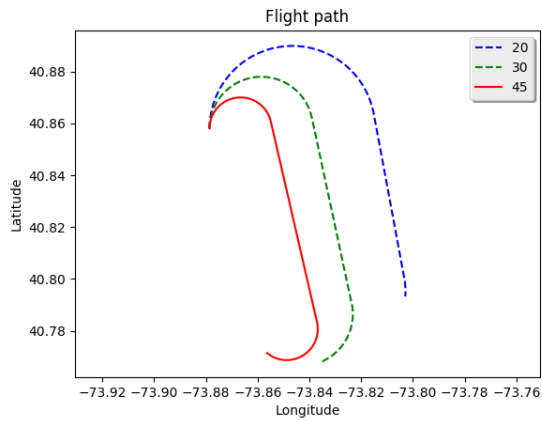
Fig. 2.47: Trajectory to LGA22 with a glide ratio of 19:1 at time $t+12$.

(a) 2D View.

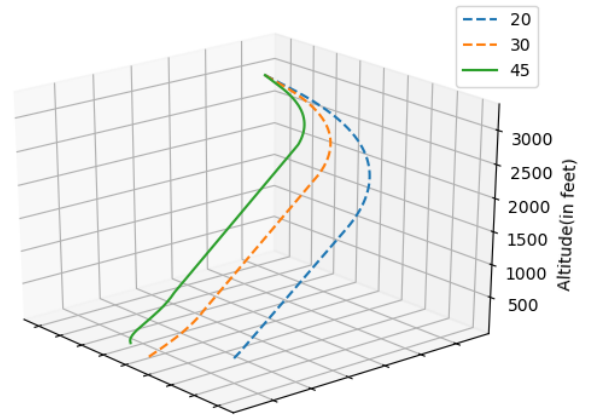


(b) 3D View.

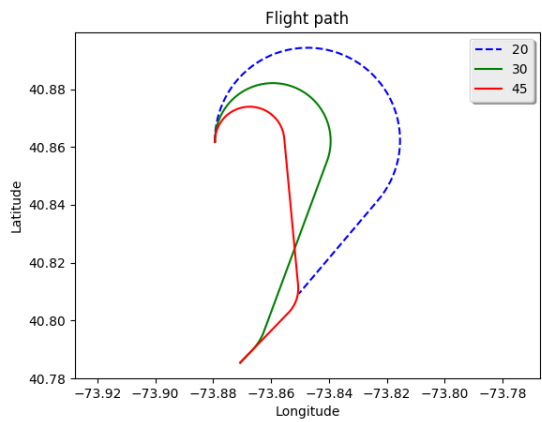
Fig. 2.48: Trajectory to LGA13 with a glide ratio of 19:1 at time $t+12$.



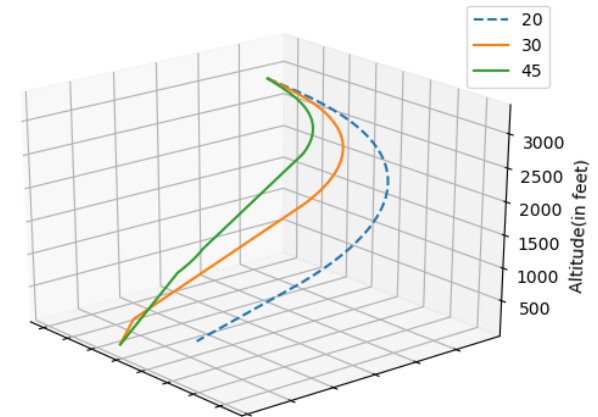
(a) 2D View.



(b) 3D View.

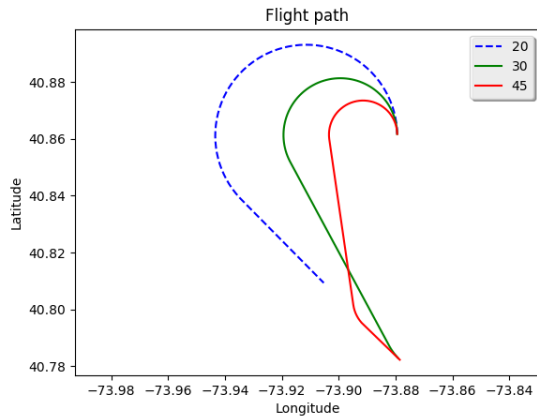
Fig. 2.49: Trajectory to LGA31 with a glide ratio of 19:1 at time $t+12$.

(a) 2D View.

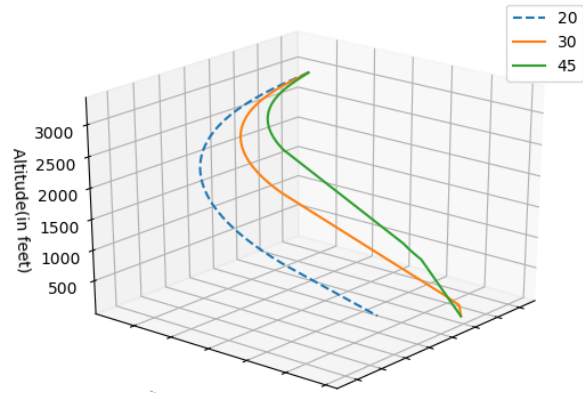


(b) 3D View.

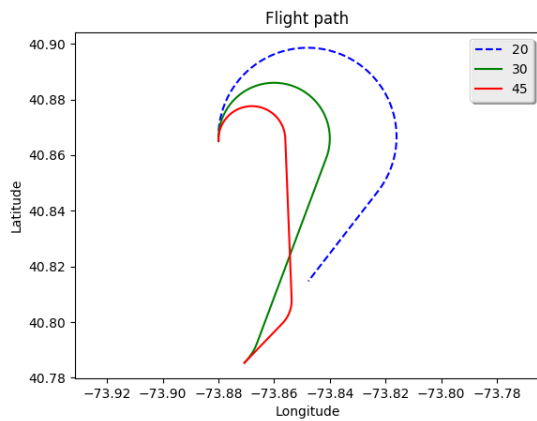
Fig. 2.50: Trajectory to LGA22 with a glide ratio of 19:1 at time $t+16$.



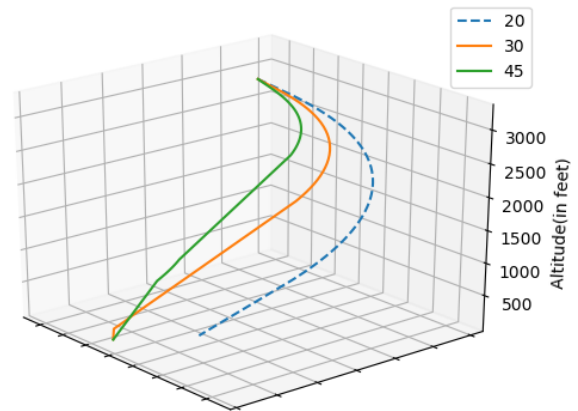
(a) 2D View.



(b) 3D View.

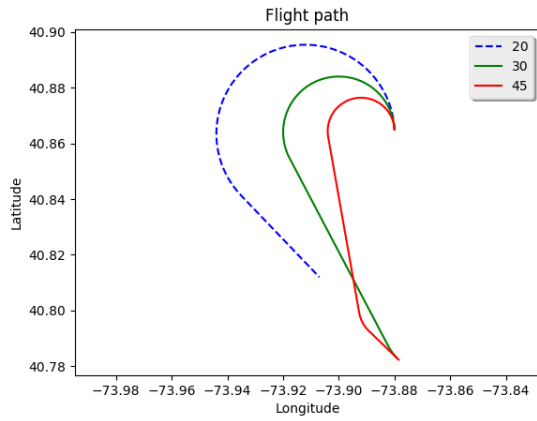
Fig. 2.51: Trajectory to LGA13 with a glide ratio of 19:1 at time $t+16$.

(a) 2D View.

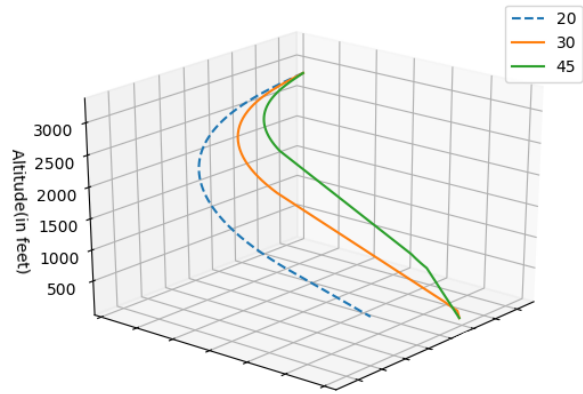


(b) 3D View.

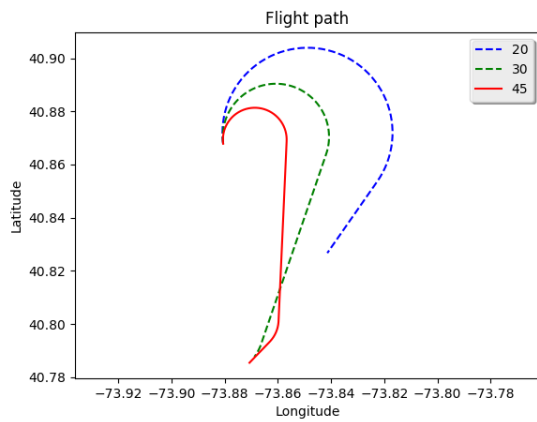
Fig. 2.52: Trajectory to LGA22 with a glide ratio of 19:1 at time $t+20$.



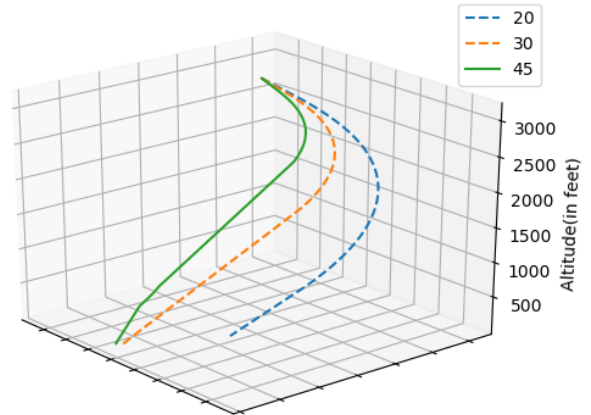
(a) 2D View.



(b) 3D View.

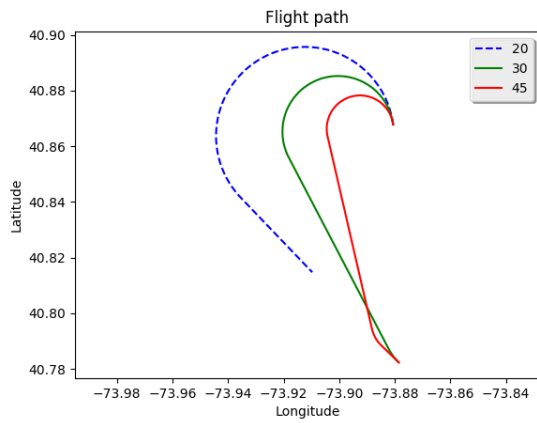
Fig. 2.53: Trajectory to LGA13 with a glide ratio of 19:1 at time $t+20$.

(a) 2D View.

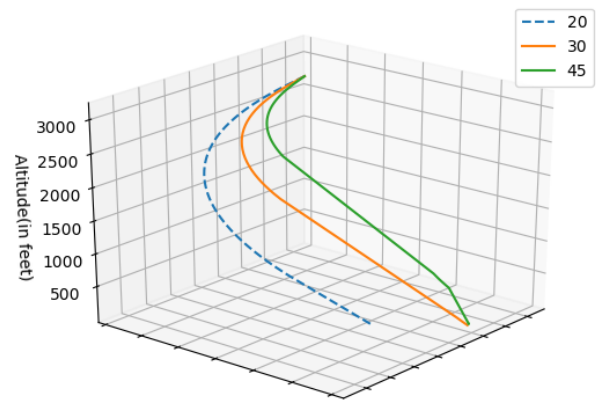


(b) 3D View.

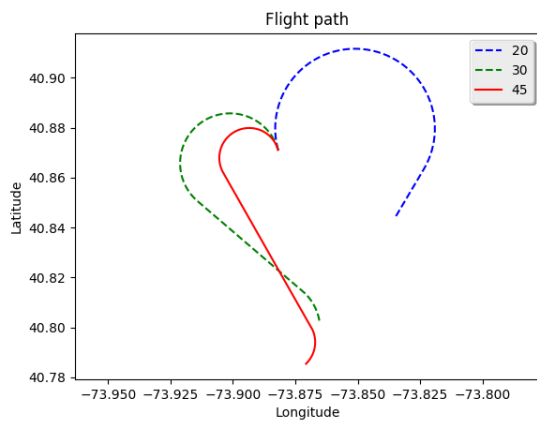
Fig. 2.54: Trajectory to LGA22 with a glide ratio of 19:1 at time $t+24$.



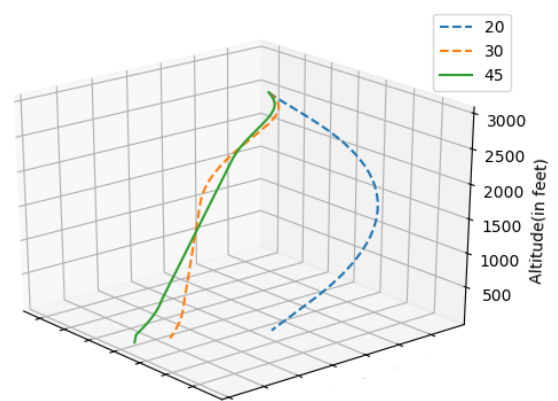
(a) 2D View.



(b) 3D View.

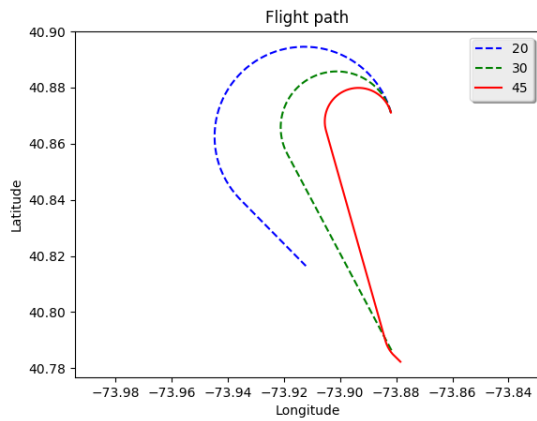
Fig. 2.55: Trajectory to LGA13 with a glide ratio of 19:1 at time $t+24$.

(a) 2D View.

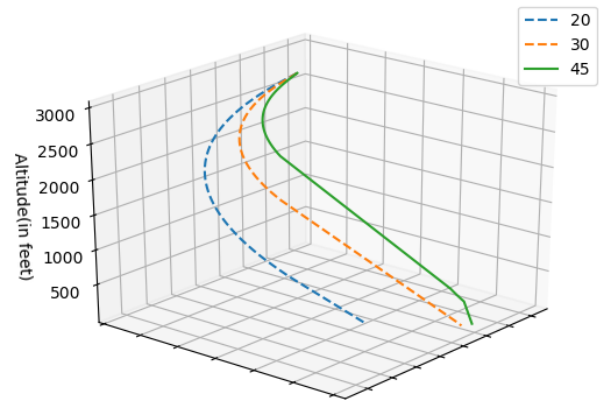


(b) 3D View.

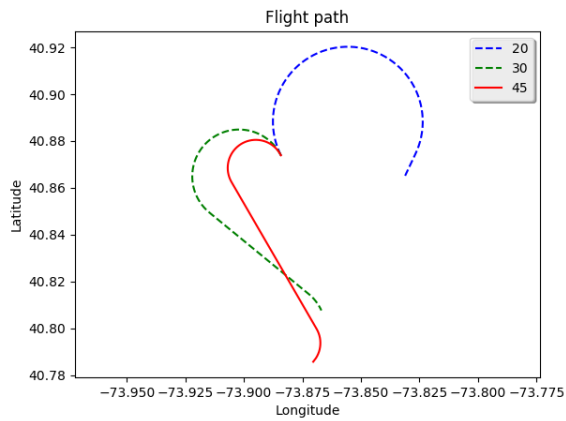
Fig. 2.56: Trajectory to LGA22 with a glide ratio of 19:1 at time $t+28$.



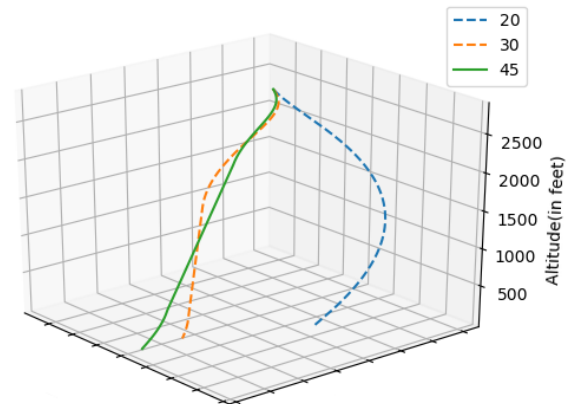
(a) 2D View.



(b) 3D View.

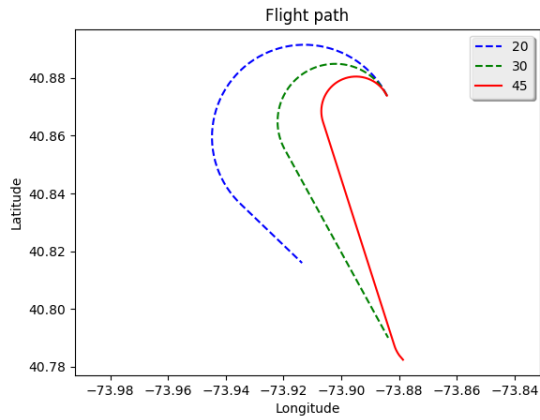
Fig. 2.57: Trajectory to LGA13 with a glide ratio of 19:1 at time $t+28$.

(a) 2D View.

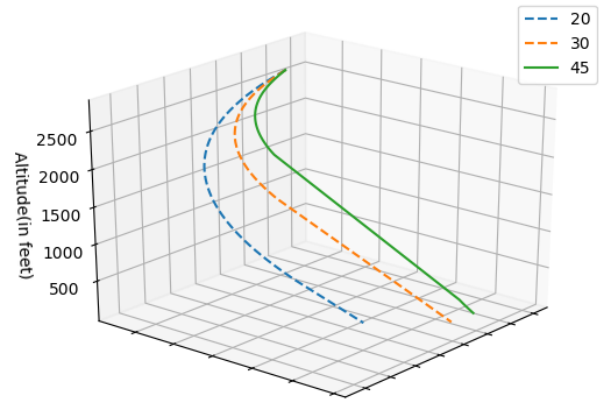


(b) 3D View.

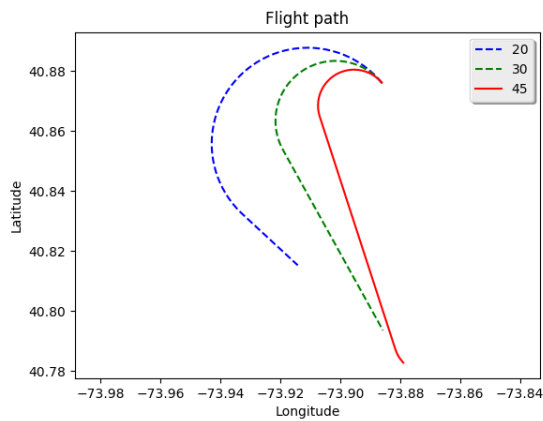
Fig. 2.58: Trajectory to LGA22 with a glide ratio of 19:1 at time $t+32$.



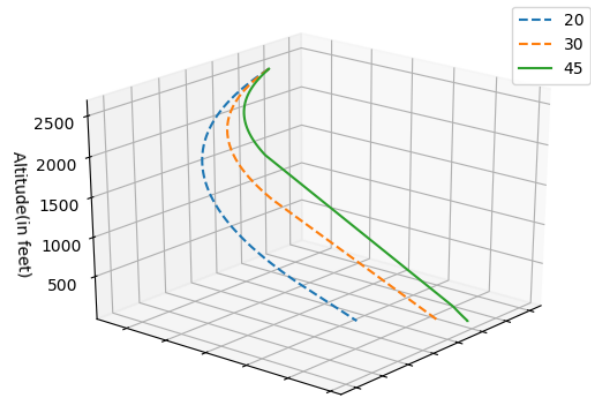
(a) 2D View.



(b) 3D View.

Fig. 2.59: Trajectory to LGA13 with a glide ratio of 19:1 at time $t+32$.

(a) 2D View.



(b) 3D View.

Fig. 2.60: Trajectory to LGA13 with a glide ratio of 19:1 at time $t+36$.

Table 2.4: Rank of trajectories for US Airways 1549 for $t+4$ to $t+24$ seconds using glide ratio 17.25:1.

Time	Runway	Bank Angle	$\ \bar{z}\ $	$\ \bar{d}\ $	$\left\ \left(\frac{\bar{\theta}}{h}\right)\right\ $	$\ \mathbf{t}\ $	$\ \mathbf{e}\ $	$\ \mathbf{n}\ $	\mathbf{u}	Rank
$t+4$	LGA22	30	0.83	0.92	1.00	1.00	0.00	1.00	0.77	3
$t+4$	LGA22	45	1.00	0.98	0.51	0.80	1.00	0.50	0.83	1
$t+4$	LGA13	45	0.93	1.00	0.63	0.82	0.67	0.50	0.78	2
$t+8$	LGA22	30	0.83	0.92	1.00	1.00	0.00	1.00	0.77	2
$t+8$	LGA22	45	1.00	0.98	0.54	0.81	1.00	0.50	0.83	1
$t+8$	LGA13	45	0.93	1.00	0.50	0.83	0.68	0.50	0.76	3
$t+12$	LGA22	30	0.84	0.94	1.00	1.00	0.00	1.00	0.78	3
$t+12$	LGA22	45	1.00	0.99	0.47	0.82	1.00	0.50	0.82	1
$t+12$	LGA13	45	0.93	1.00	0.63	0.84	0.69	0.50	0.79	2
$t+16$	LGA22	30	0.85	0.92	1.00	1.00	0.00	1.00	0.77	3
$t+16$	LGA22	45	1.00	0.99	0.45	0.82	1.00	0.50	0.82	1
$t+16$	LGA13	45	0.95	1.00	0.63	0.83	0.72	0.50	0.80	2
$t+20$	LGA22	45	1.00	0.99	0.80	0.99	1.00	1.00	0.96	1
$t+20$	LGA13	45	0.95	1.00	1.00	1.00	0.00	1.00	0.81	2
$t+24$	LGA22	45	0.98	1.00	0.38	1.00	1.00	1.00	0.88	2
$t+24$	LGA13	45	1.00	0.98	1.00	0.99	1.00	1.00	1.00	1
$t+28$	LGA13	45	1.00	1.00	1.00	1.00	1.00	1.00	1.00	1

Using a glide ratio of 17.25:1, LGA4 and LGA31 were not reachable at any time, LGA22 was reachable upto $t + 24$ seconds, and LGA13 was reachable until $t + 28$ seconds.

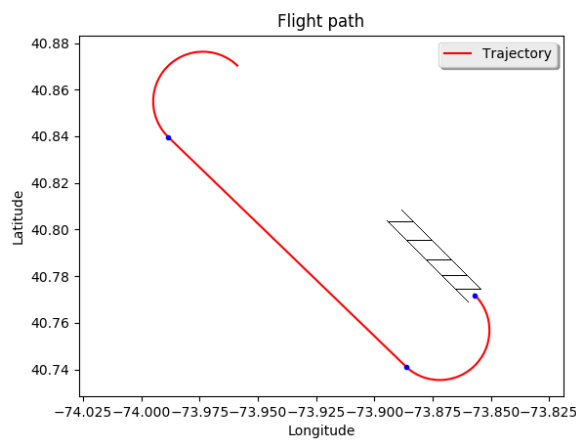
Using a glide ratio of 19:1, LGA4 was never reachable, LGA31 was reachable upto $t + 12$ seconds, LGA22 was reachable upto $t + 32$ seconds, and LGA13 was reachable for the longest time, until $t + 36$ seconds.

We implemented our safety metrics to rank the trajectories generated with a glide ratio of 17.25:1 (Table. 2.4). For calculating the utility function, we assigned a weight of 1 to the number of turns metric and a weight of 2 to all the other metrics. For a given runway, the 45° trajectory usually ranked better than the 30° trajectory according to our metrics, while a 20° bank angle always failed to produce a valid trajectory.

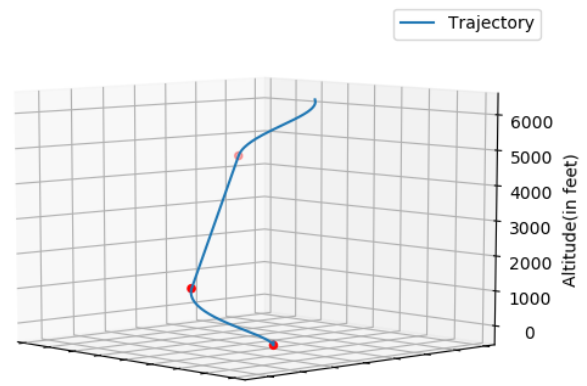
Therefore, we can see that feasible trajectories to LGA13 could be generated at least until $t + 28$ seconds after the birds strike. If this information was made available to the pilots during the actual emergency of flight 1549, perhaps a water landing could have been avoided. Moreover, the ranking of trajectories would have allowed the pilots to swiftly decide on the best trajectory for landing the aircraft safely.

2.7.3 Analysis of The Minimum Altitude of Return for an Airbus A320

We further performed an experiment to determine the minimum altitude of return for an Airbus A320, taking off from a runway of length 2190 m with a climb speed of 175 knots and a climb rate of 2500 feet per minute. For landing on the same runway in the takeoff configuration, with a bank angle of 30° , the minimum altitude from which this would be achievable was found to be approximately 6150 feet (Fig. 2.61). On the other hand, for landing on the opposite end of the same runway, in the reverse configuration, the minimum required altitude was found to be approximately 3485 feet (Fig. 2.62).

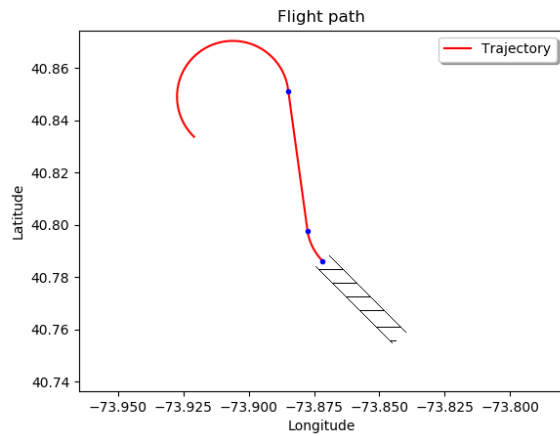


(a) 2D view.

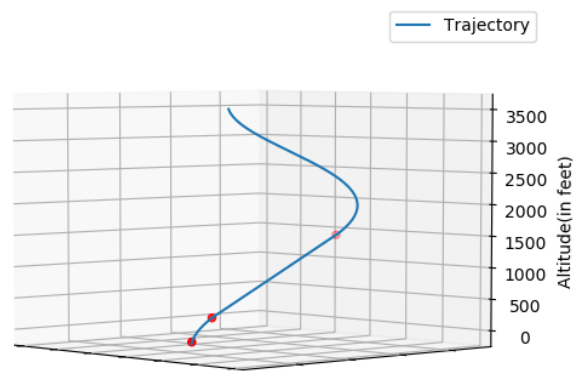


(b) 3D view.

Fig. 2.61: Minimum altitude for returning to take-off configuration (A320).



(a) 2D view.



(b) 3D view.

Fig. 2.62: Minimum altitude for returning to opposite end of runway (A320).

CHAPTER 3

Wind-Aware Trajectory Generation

3.1 Background

In the previous chapter, we have investigated dynamic data-driven avionics software in decision support systems for loss-of-thrust emergency scenarios. We presented a system for generating feasible trajectories for LOT scenarios by distilling a complex aerodynamic model to two variables: glide ratio and radius of turn for discrete bank angles and drag configurations. However, the algorithm does not consider the effect of wind while generating trajectories to nearby runways. In this chapter, we present a wind model for modeling the effect of a constant horizontal wind vector (\vec{w}) on a trajectory. This wind model can be used by our dynamic data-driven component to predict the effect of wind and generate high fidelity wind-aware trajectories that can bring a gliding aircraft down to a target runway.

We define an *air trajectory* to be a three-dimensional path with respect to the moving airmass while its corresponding *ground trajectory* is the three-dimensional projection with respect to the ground frame of reference. A *no-wind air trajectory* to a target runway is not corrected for wind and might take an aircraft away from the runway. Our approach generates a *wind-aware air trajectory* to a *virtual runway* – a point that lies on the wind vector passing through the actual target runway. The ground trajectory of this wind-aware air trajectory can successfully bring an aircraft down to the target runway, if the aircraft always maintains the best gliding airspeed. We present an analytical approach for computing the required position of the virtual runway and a heuristic iterative approach for cases which are not considered by our analytical approach. We make decision making easy for the pilots by providing them with trajectories that consist of a series of standard maneuvers (constant-bank turns and straight line gliding segments).

Portions of this chapter previously appeared as: S. Paul, F. Hole, A. Zyteck, and C. A. Varela. “Wind-aware trajectory planning for fixed-wing aircraft in loss of thrust emergencies.” in *Proc. of the 37th AIAA/IEEE Digit. Avionics Syst. Conf.*, London, England, UK, September 2018, pages 558-567.

Portions of this chapter have been submitted to: S. Paul and C. A. Varela. “Data-Driven Wind-Aware Emergency Trajectory Planning for Fixed-Wing Aircraft.” in *J. Aircraft*.

3.2 Chapter Contributions

The following items represent our original research contributions as presented in this chapter:

- Our wind-model for predicting the effect of wind on trajectories (Section 3.3).
- Our wind-aware trajectory generation algorithm with analytical and iterative solutions (Section 3.4).
- Experimental evaluation of our approach. (Section 3.5).

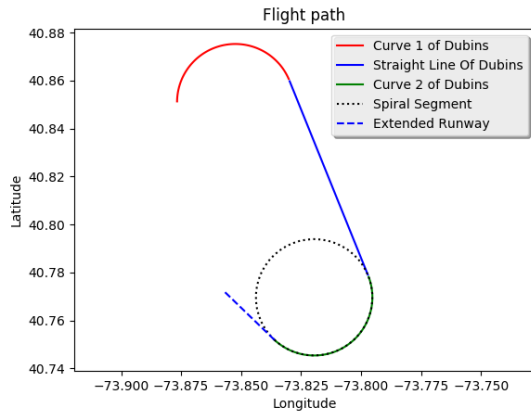
3.3 Modeling the Effect of Wind on Trajectories

In the case of a LOT emergency, the nature of trajectories depends upon several factors – the baseline glide ratio of the aircraft, the aircraft airspeed, the heading and location of the emergency, the heading and location of the runway and the wind conditions. In [3], we have defined valid no-wind air trajectories that take into account all of the above factors except for the wind conditions. These no-wind air trajectories consist of three-dimensional Dubins paths followed by spiral maneuvers and extended runway segments. The presence of wind can significantly alter the ground trajectories of these air trajectories. In this section, we model the effect of horizontal wind on an air trajectory.

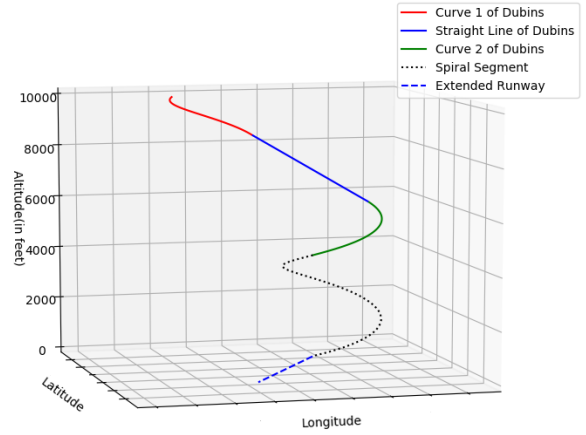
There are five unique segments of a trajectory as defined in [3] (Fig. 3.1). They are:

1. Curve 1 of the Dubins path - $\mathcal{C}1$.
2. Straight Line Segment of the Dubins Path - $\mathcal{S}1$.
3. Curve 2 of the Dubins path - $\mathcal{C}2$.
4. Spiral Segment - $\mathcal{C}3$.
5. Extended Runway Segment - $\mathcal{S}2$.

Each of these segments (if present) in a trajectory is affected in a different way. Hence, in order to model the effect of wind on the entire trajectory, we need to model the effect of wind on each segment independently and calculate the amount of shift (ψ) of the endpoint, the time (t) of flight and the total altitude loss (δz) for each of them.

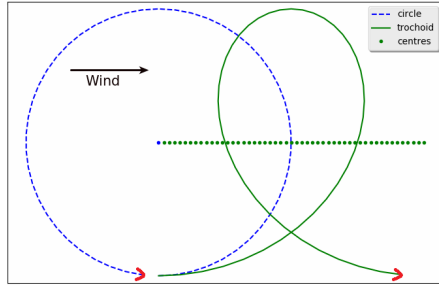


(a) 2D view of a typical trajectory.

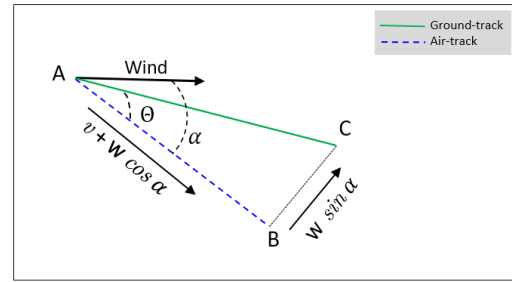


(b) 3D view of a typical trajectory.

Fig. 3.1: Parts of a trajectory.



(a) Effect of wind on turns.



(b) Effect of wind on straight line glide.

Fig. 3.2: Effect of wind on turns and straight line glide.

Aircraft paths are composed of two basic movements: banked turns and straight line segments. In the case of banked turns, the original circular arcs are affected by the wind to produce trochoidal tracks above the ground. A trochoid (Fig. 3.2a) is a geometrical figure that is formed by the locus of a fixed point (x, y) on the circumference of a circle, the centre (c_x, c_y) of which moves along a straight line. The general equations which define a point on a trochoid are:

$$x(t) = c_x(t) + r \cos \phi \quad (3.1)$$

$$y(t) = c_y(t) + r \sin \phi \quad (3.2)$$

$$c_x(t) = c_{x_0} + (w_x \times t) \quad (3.3)$$

$$c_y(t) = c_{y_0} + (w_y \times t) \quad (3.4)$$

where ϕ is the angular distance of the point from the centre, (c_{x_0}, c_{y_0}) is the initial center and (w_x, w_y) are the velocities of the movement of the center in the two-dimensional plane given the horizontal wind vector $\vec{w}(w, \lambda_w)$.

In the case of straight line segments, the aircraft still follows a linear path with respect to the ground, but the actual direction of that line is different from the original intended path (Fig. 3.2b). The new path can be calculated by calculating the lateral shift (ψ) arising due to the crosswind component of the wind:

$$\psi = w \sin \alpha \times t \quad (3.5)$$

where t is the time taken to fly the intended linear path, α is the angle between the heading of the aircraft and the wind direction and $w \sin \alpha$ is the crosswind component.

3.3.1 Effect of Wind on Turns

Let the initial and final points of the airmass curve \mathcal{C} be $(x_i, y_i, z_i, \lambda_i)$ and $(x_f, y_f, z_f, \lambda_f)$ respectively where x , y , z and λ represent the latitude, longitude, altitude and heading of the aircraft at a point. If the radius of turn is r (Eq. 2.18), then the inscribed angle of \mathcal{C} is given by:

$$\Delta\phi = \cos^{-1} \left(1 - \frac{(x_i - x_f)^2 + (y_i - y_f)^2}{2 \times r^2} \right) \quad (3.6)$$

The time taken t_c can now be derived as:

$$t_c = \frac{\Delta\phi \times r}{v} \quad (3.7)$$

where v is the aircraft airspeed. Therefore, the total shift of the center of rotation for $\widehat{\mathcal{C}}$, which is the ground trajectory of \mathcal{C} , is given by:

$$\psi_c = t_c \times w \quad (3.8)$$

Now, the *ground glide ratio* $g_e(t)$ (the glide ratio with respect to the ground) throughout $\widehat{\mathcal{C}}$ is given by:

$$g_e(t) = g_0 \times \cos \theta \times \frac{(v_g)}{v} \quad (3.9)$$

where $v_g(t)$ is the ground-speed given by:

$$v_g(t) = v + (w \times \cos \alpha(t)) \quad (3.10)$$

where $\alpha(t) = (\lambda_v(t) - \lambda_w)$ and $\lambda_v(t)$ is the direction of the aircraft airspeed which varies with time in a turn.

Therefore, the total loss in altitude $(\delta z)_{\hat{C}}$ in \hat{C} is given by:

$$(\delta z)_{\hat{C}} = z_i - z_f \quad (3.11)$$

The above model applies to parts $\mathcal{C}1$, $\mathcal{C}2$ and $\mathcal{C}3$ of a trajectory which are all constant-bank turns.

3.3.2 Effect of Wind on Straight Line Segments

Let the initial and final points of a straight line part of the no-wind trajectory be $A = (x_A, y_A, z_A, \lambda_A)$ and $B = (x_B, y_B, z_B, \lambda_A)$ respectively (Fig. 3.2b). Therefore, the original straight line part of the no-wind air trajectory is \overrightarrow{AB} , represented by \mathcal{S} . Now, let the final point of the straight line part in the corresponding ground trajectory $\hat{\mathcal{S}}$ be $C = (x_C, y_C, z_C, \lambda_A)$. Time (t_S) required to cover distance \overrightarrow{AB} is given by:

$$t_S = \frac{|\overrightarrow{AB}|}{v} \quad (3.12)$$

We know that the heading of aircraft airspeed throughout \overrightarrow{AC} is λ_A . Therefore, the ground-speed throughout the \overrightarrow{AC} is given by:

$$v_g = v + w \times \cos \alpha \quad (3.13)$$

where $\alpha = \lambda_A - \lambda_w$.

Therefore, the new distance $|\overrightarrow{AC}| = t_S * v_g$. Let the angle between \overrightarrow{AB} and \overrightarrow{AC} be Θ .

$$\Theta = \tan^{-1} \frac{w \times \sin \alpha}{v} \quad (3.14)$$

The shift $|\overrightarrow{BC}|$ is given by:

$$|\overrightarrow{BC}| = t_S \times w \times \sin \alpha = \psi_S \quad (3.15)$$

The total loss in altitude is given by:

$$\delta z_{\hat{S}} = z_A - z_C = z_A - \frac{|\overrightarrow{AC}|}{g_e} \quad (3.16)$$

where g_e is the ground glide ratio in the straight line segment given by:

$$g_e = g_0 \times \frac{v_g}{v} \quad (3.17)$$

The above model applies to parts $\mathcal{S}1$ and $\mathcal{S}2$ of a trajectory as both represent straight line gliding.

3.4 Wind-Aware Trajectory Generation

When an aircraft follows a no-wind air trajectory with respect to the airmass, in the presence of wind, the resultant ground trajectory is significantly different. For a wind-aware trajectory to be able to successfully lead a gliding aircraft to a target runway, two conditions have to be met:

- Condition I: *The trajectory must be able to bring the aircraft down to the altitude of the runway.*

In order for the ground trajectory of a no-wind air trajectory to bring the aircraft down to the required altitude, the total loss in altitude should be equal to the difference between the altitude of the initial position of the aircraft and the altitude of the target runway.

$$(\delta z)_{C1} + (\delta z)_{S1} + (\delta z)_{C2} + (\delta z)_{C3} + (\delta z)_{S2} = \Delta z \quad (3.18)$$

where Δz is the altitude difference between the initial configuration of the aircraft and the target runway.

- Condition II: *The end of the trajectory must meet the coordinates of the runway in the two-dimensional space.*

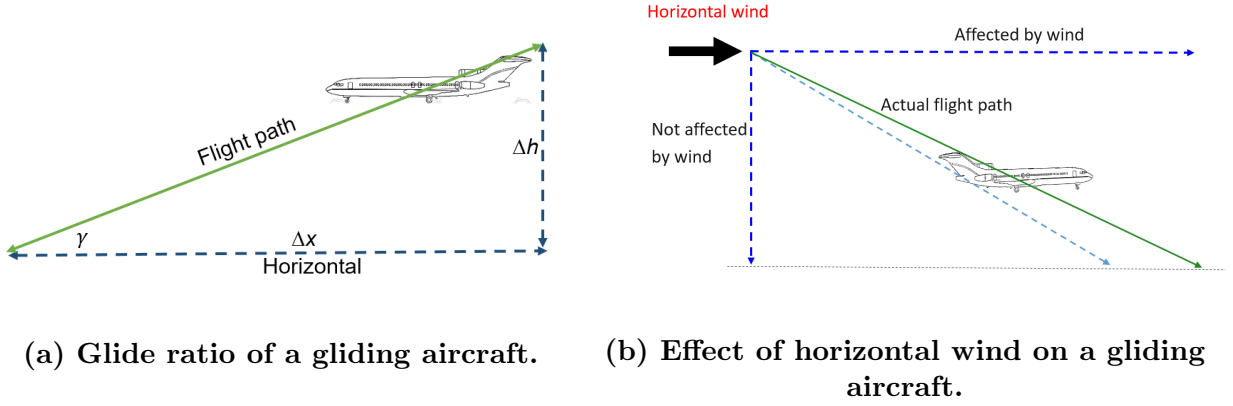


Fig. 3.3: Effect of horizontal wind on glide ratio.

In the presence of wind, the ground trajectory of a no-wind air trajectory changes significantly as described in the previous section. It has been previously demonstrated in [9] that in the presence of a constant horizontal wind, the final position of the ground trajectory lies on a line which is parallel to the wind vector and passes through the endpoint of the no-wind air trajectory. Therefore, the problem of finding a wind-aware air trajectory is distilled to the problem of intercepting a virtual target moving away from the actual runway in the upwind direction.

Therefore, if T is the total time of flight for the original no-wind trajectory, for the wind augmented trajectory to intercept the runway, the following condition must be met:

$$\psi_{C1} + \psi_{S1} + \psi_{C2} + \psi_{C3} + \psi_{S2} = T \times w \quad (3.19)$$

Now, we know that,

$$T = t_{C1} + t_{S1} + t_{C2} + t_{C3} + t_{S2} \quad (3.20)$$

Therefore,

$$(t_{C1} + t_{S1} + t_{C2} + t_{C3} + t_{S2}) \times w = \psi_{C1} + \psi_{S1} + \psi_{C2} + \psi_{C3} + \psi_{S2} \quad (3.21)$$

In the presence of wind, the ground glide ratio of a gliding aircraft is different from the aerodynamic glide ratio (Eq. 3.9, Eq. 3.17), but the *rate of descent* (σ) remains unaffected by horizontal wind (Fig. 3.3b). Therefore, if an aircraft glides with the best gliding airspeed for time t , then the loss of altitude will always be equal to σt , even though the horizontal

distance covered will be different in case of tailwind, headwind, and no - wind conditions.

$$\Delta z(t) = \sigma t \quad (3.22)$$

Therefore, in order to compute valid wind-aware air trajectories, we make the following assumptions:

1. The aircraft always flies with the best gliding airspeed v .
2. For each segment in an air trajectory, time t is required to fly that segment with respect to the airmass.
3. The aircraft follows each segment of the air trajectory for time t .

Assumptions 1, 2 and 3 imply that a ground trajectory will lose exactly the same amount of altitude as the corresponding air trajectory since the time in air is equal for both. This ensures that Condition I holds. Therefore, the problem of generating a wind-aware air trajectory is reduced to the problem of generating a no-wind air trajectory, the ground trajectory of which can bring an aircraft to the correct position in the horizontal plane: $R = (x, y, \lambda)$. This can be achieved by generating a wind-aware air trajectory to a virtual runway $R' = (x', y', \lambda' = \lambda)$ in the horizontal plane such that Condition II (Eq. 3.21) is met.

3.4.1 Analytical Solution for Finding R'

For being able to analytically compute the location of the virtual runway, we need to be able to predict the total shift caused by the various segments of the trajectory. In order to simplify the task of prediction, we first generate an initial no-wind air trajectory (P) to the actual runway to model the effect of wind on it and then compute a new wind-aware air trajectory to a virtual runway that has the same type of initial Dubins path, the same integral number of spirals, and an extended runway segment that has the same length and orientation with respect to the wind vector. This allows us to compute ψ_{C1} , ψ_{C2} , ψ_{C3} , ψ_{S1} , and ψ_{S2} for P and argue that for the new wind-aware air trajectory P' , $\psi_{C3'}$ and $\psi_{S2'}$ will have the same value as that of ψ_{C3} and ψ_{S2} respectively. This is because the same integral number of spirals will always produce the same amount of shift in the presence of a constant horizontal wind, irrespective of their position and two extended runway segments of equal length and orientation with respect to the wind vector will also produce the same shift.

The total shift $\Psi(P')$ caused by the effect of wind on P' is given by:

$$\Psi(P') = \psi_{C1'} + \psi_{C2'} + \psi_{S1'} + \psi_{C3'} + \psi_{S2'} \quad (3.23)$$

For a trajectory in the horizontal plane to be valid, it must satisfy the following constraint, which follows directly from Condition II:

$$\Psi(P') = |\overline{RR'}| \quad (3.24)$$

Since P and P' have similar $C3$ and $S2$, the end point of $C2'$ should lie on a line passing through the end point of $C2$ in the upwind direction. Hence, a valid P' satisfies the following condition:

$$\Psi(P') - (\psi_{C3'} + \psi_{S2'}) = \psi_{C1'} + \psi_{C2'} + \psi_{S1'} = |\overline{ee'}| \quad (3.25)$$

where e and e' are the end points of $C2$ and $C2'$.

For trajectories whose initial Dubins paths are of the form *left - straight - left* or *right - straight - right*, the total heading change and thus the total curve length of $C1$ and $C2$ is the same for all variations of trajectories given that the aforementioned constraints are satisfied. Hence we can conclude that:

$$\psi_{C1'} + \psi_{C2'} = \psi_{C1} + \psi_{C2} \quad (3.26)$$

Therefore, from equations 3.25 and 3.26, we get

$$|\overline{ee'}| = (\psi_{C1} + \psi_{C2}) + \psi_{S1'} \quad (3.27)$$

Let the lengths of $S1$ and $S1'$ be l and l' respectively and the angle between the heading of $S1$ and \vec{w} be α and the angle between the heading of $S1'$ and \vec{w} be α' (Fig. 3.4a). Now, time to fly $S1'$ is given by:

$$t_{S1'} = \frac{l'}{v + w \cos \alpha'} \quad (3.28)$$

and

$$\psi_{S1'} = t_{S1'} \times w \sin \alpha' \quad (3.29)$$

Since the total heading change and thus the total curve length of $(C1 + C2)$ and $(C1' + C2')$

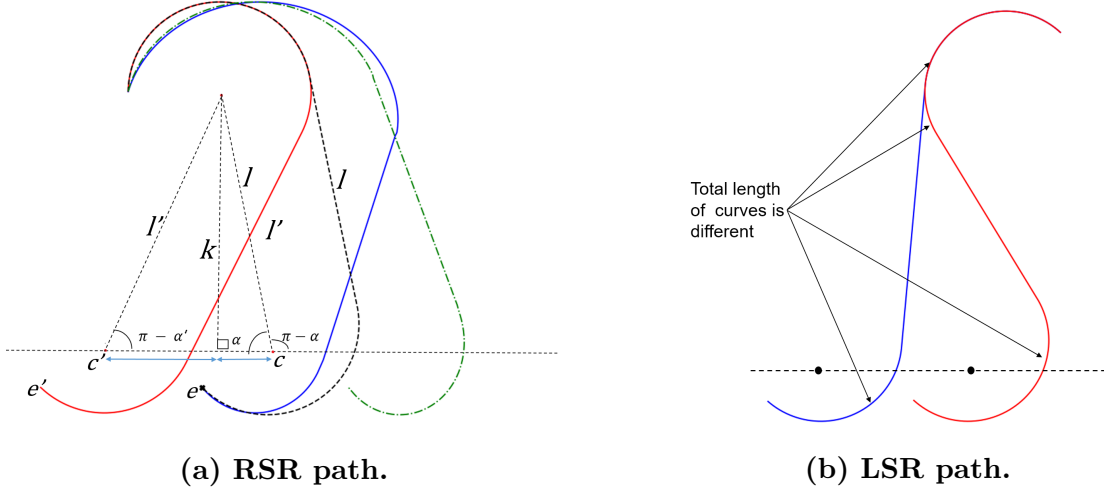


Fig. 3.4: Geometry of RSR (symmetrical to LSL) and LSR (symmetrical to RSL) paths.

are the same, therefore, $(\delta z)_{c_1} + (\delta z)_{c_2} = (\delta z)_{c_{1'}} + (\delta z)_{c_{2'}}$. By construction, the total change in altitude for the entire Dubins path segments of P and P' are equal. Therefore,

$$\begin{aligned}
 (\delta z)_{c_1} + (\delta z)_{c_2} + (\delta z)_{s_1} &= (\delta z)_{c_{1'}} + (\delta z)_{c_{2'}} + (\delta z)_{s_{1'}} \\
 \text{or, } (\delta z)_{s_1} &= (\delta z)_{s_{1'}} \\
 \text{or, } \sigma t_{s_{1'}} &= \sigma t_{s_1} \text{ (from Eq. 3.22)} \\
 \text{or, } t_{s_{1'}} &= t_{s_1}
 \end{aligned} \tag{3.30}$$

From symmetry (Fig. 3.4a), distance between the end points of C_2 and $C_{2'}$ ($|\overline{ee'}|$) is equal to the distance between their centres ($|\overline{cc'}|$). Hence, from equations 3.27 and 3.29, we get:

$$|\overline{cc'}| = \psi_{s_{1'}} + (\psi_{c_1} + \psi_{c_2}) = (t_{s_{1'}} \times w \sin \alpha') + (\psi_{c_1} + \psi_{c_2}) \tag{3.31}$$

From geometry, we can see that (Fig. 3.4a),

$$|\overline{cc'}| = k \left(\frac{1}{\tan \alpha} - \frac{1}{\tan \alpha'} \right) \tag{3.32}$$

where k is the perpendicular distance between the centre of C_1 and the line parallel to \vec{w}

and passing through c . Therefore,

$$(t_{S1'} \times w \sin \alpha') + (\psi_{C1} + \psi_{C2}) = k \left(\frac{1}{\tan \alpha} - \frac{1}{\tan \alpha'} \right) \quad (3.33)$$

Let $K_1 = t_{S1'} \times w$, $K_2 = (\psi_{C1} + \psi_{C2})$ and $K_3 = \frac{k}{\tan \alpha} - K_2$. These are values that can be pre-computed by modeling the effect of wind on P . Therefore, we get:

$$\begin{aligned} K_1 \sin \alpha' + K_2 &= \frac{k}{\tan \alpha} - \frac{k}{\tan \alpha'} \\ \text{or, } K_1 \sin \alpha' + k \frac{\sin \alpha'}{\cos \alpha'} &= \frac{k}{\tan \alpha} - K_2 \\ \text{or, } K_1 \sin \alpha' + k \frac{\sin \alpha'}{\cos \alpha'} &= K_3 \end{aligned} \quad (3.34)$$

which can be expanded into the following quartic equation in terms of $\sin \alpha'$:

$$K_1^2 \sin^4 \alpha' - 2K_1 K_3 \sin^3 \alpha' + (K_3^2 + k^2) \sin^2 \alpha' - k^2 = 0 \quad (3.35)$$

From Fig. 3.4a, we can see that $l' = k / \sin \alpha'$. Therefore, from Eq. 3.28, we get:

$$\begin{aligned} t_{S1'} &= \frac{l'}{v + w \cos \alpha'} \\ \text{or, } t_{S1'} &= \frac{k}{\sin \alpha' (v + w \cos \alpha')} \\ \text{or, } k &= t_{S1'} \times \sin \alpha' (v + w \cos \alpha') \\ \text{or, } k &= t_{S1'} \times v \sin \alpha' + t_{S1'} \times w \sin \alpha' \cos \alpha' \\ \text{or, } k &= K_4 \sin \alpha' + K_1 \sin \alpha' \cos \alpha' \end{aligned} \quad (3.36)$$

where $K_4 = t_{S1'} \times v$. The above equation can be expanded into another quartic equation in $\sin \alpha'$:

$$K_1^2 \sin^4 \alpha' + (K_4^2 - K_1^2) \sin^2 \alpha' - 2K_4 k \sin \alpha' + k^2 = 0 \quad (3.37)$$

Since we have two quartic equations, it now becomes possible to derive the following cubic equation in terms of $\sin \alpha'$ from equations 3.35 and 3.37:

$$2K_1 K_3 \sin^3 \alpha' + (K_4^2 - K_1^2 - K_3^2 - k^2) \sin^2 \alpha' - 2K_4 k \sin \alpha' + 2k^2 = 0 \quad (3.38)$$

Since a cubic equation always has a real root, a real value of $\sin \alpha'$ can be computed from Eq. 3.38 which can be used to calculate $|\overline{cc'}|$ and therefore $|\overline{ee'}|$ using Eq. 3.31. Finally, we can compute the shift of P' by using Eq. 3.25, which is the required distance of the virtual target from the actual runway in the upwind direction.

The above approach, however, cannot be implemented for trajectories whose initial Dubins paths are of the type *right - straight - left* or *left - straight - right*. This is because in these types of Dubins paths, the total curve length of $\mathcal{C}1$ and $\mathcal{C}2$ differ for different variations (Fig. 3.4b). This makes us unable to use $\psi_{\mathcal{C}1} + \psi_{\mathcal{C}2}$ calculated from P as a constant in P' .

3.4.2 Iterative Solution for Finding R'

```

find_virtual_runway(initial_no_wind, runway, wind_heading)
    initial_wind = model_wind(initial_no_wind)
    last_point = final_point(initial_wind)
    deviation = difference(runway, last_point)
    distance = 0
    virtual_point = null
    while(deviation > 0)
        distance = distance + deviation
        reverse_wind_heading = reverse(wind_heading)
        virtual_point = along_heading_at_distance(runway, reverse_wind_heading,
        ↪ distance)
        temp_no_wind = find_no_wind_air_trajectory(virtual_point)
        temp_wind = model_wind(temp_no_wind)
        temp_last_point = final_point(temp_wind)
        deviation = difference(runway, temp_last_point)
    return virtual_point

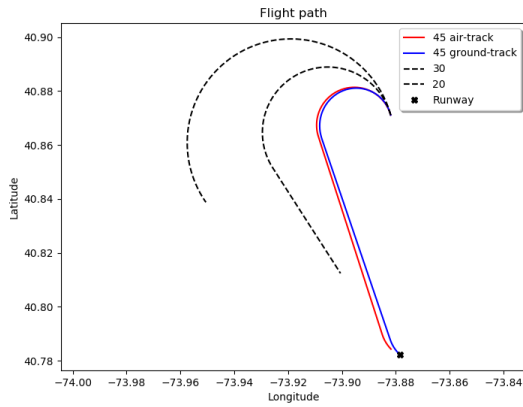
```

Pseudocode 3.1. Heuristic iterative approach for computing R'

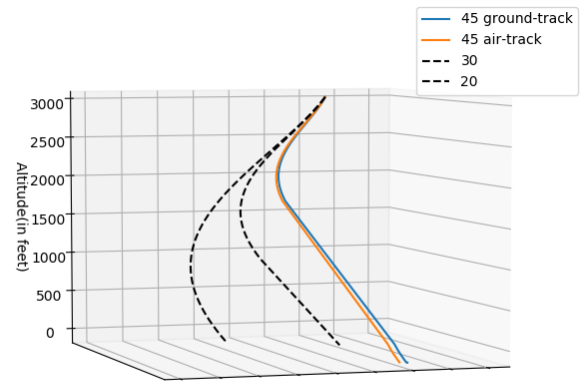
When the analytical solution for finding R' cannot be applied, we can use a heuristic iterative approach for computing R' as given in Pseudo-code 3.1.

3.5 Experimentation and Results

We considered the US Airways 1549 incident as a use case for our simulations. At the time of the incident, a 9 kts wind was blowing from approximately 300 degrees. As mentioned in Chapter 2, trajectories could be computed up to $t + 28$ and $t + 36$ seconds using glide ratios 17.25 : 1 and 19 : 1 respectively. We simulated these two trajectories with the actual wind conditions (Fig. 3.5 and Fig. 3.6).

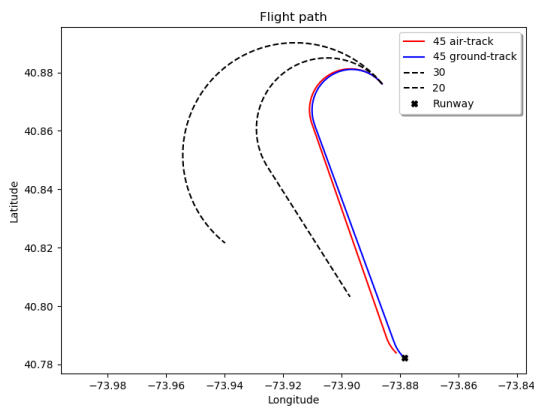


(a) 2D View.

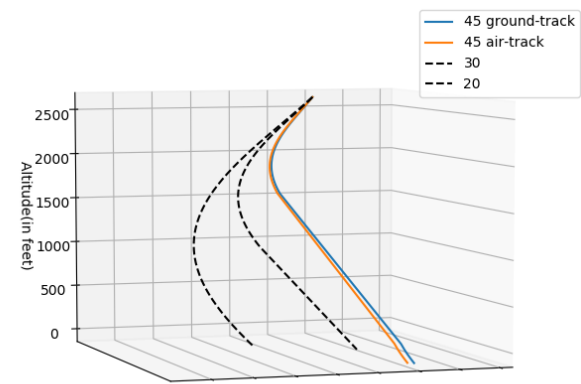


(b) 3D View.

Fig. 3.5: Wind-aware trajectory to LGA13 with a glide ratio of 17.25:1, 28 seconds after birds strike.

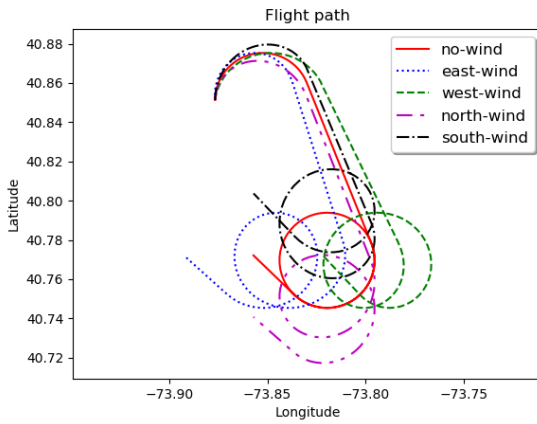


(a) 2D View.

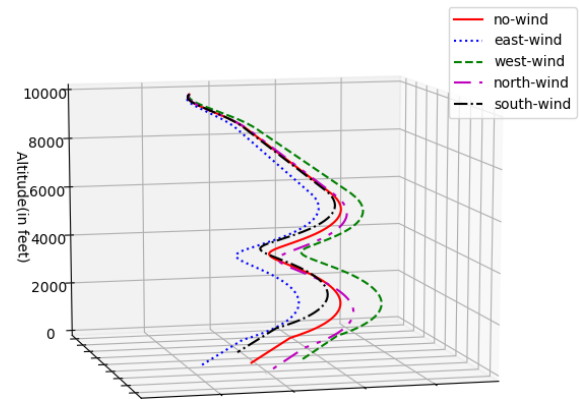


(b) 3D View.

Fig. 3.6: Wind-aware trajectory to LGA13 with a glide ratio of 19:1, 36 seconds after birds strike.

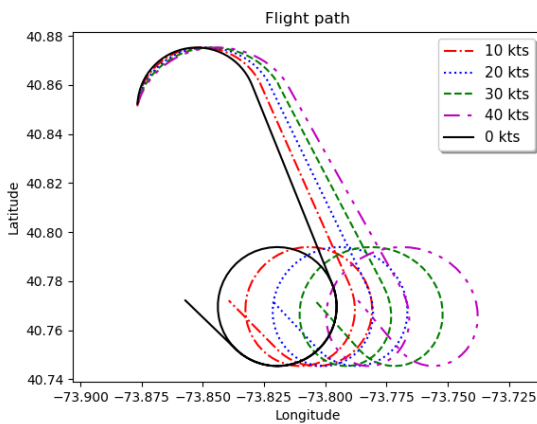


(a) 2D view.

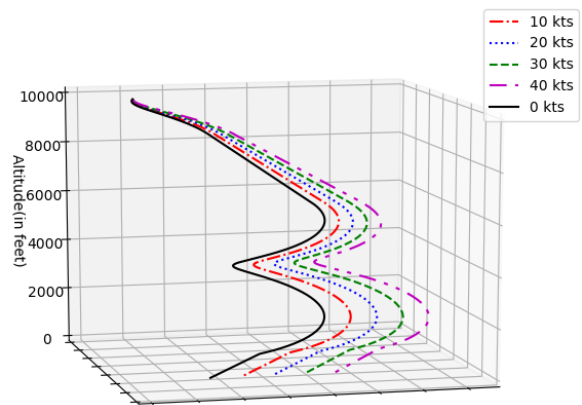


(b) 3D view.

Fig. 3.7: Effect of a 40 knot wind from different directions on a trajectory from 10000 feet.

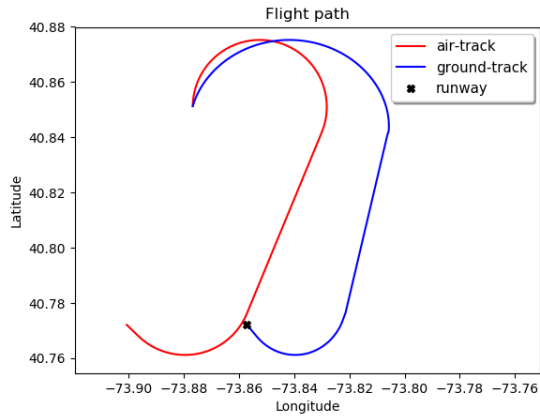


(a) 2D view.

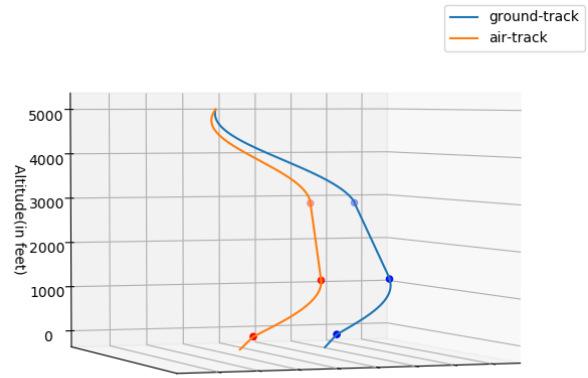


(b) 3D view.

Fig. 3.8: Effect of different magnitudes of West-wind on a trajectory from 10000 feet.

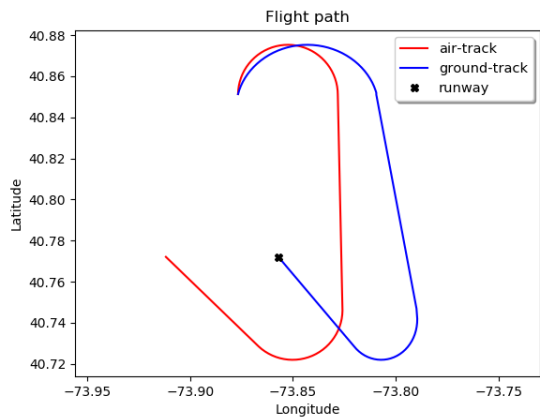


(a) 2D view.

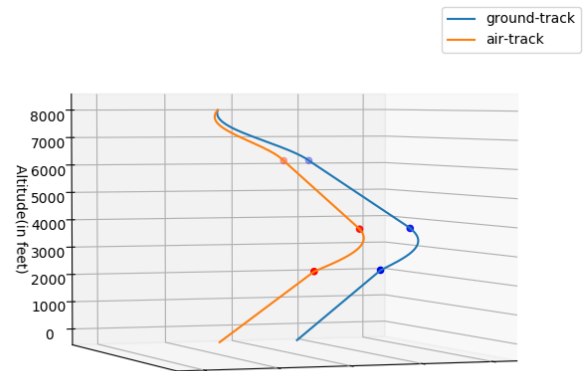


(b) 3D view.

Fig. 3.9: Wind-aware trajectory from 5000 feet in 40 knots West-wind.

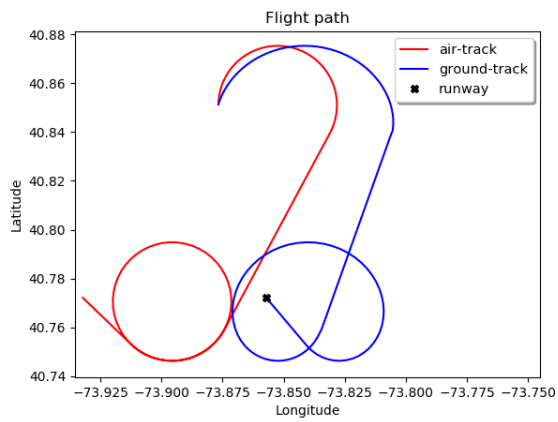


(a) 2D view.

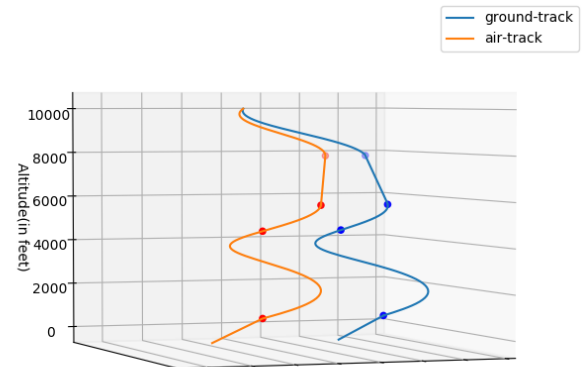


(b) 3D view.

Fig. 3.10: Wind-aware trajectory from 8000 feet in 40 knots West-wind.

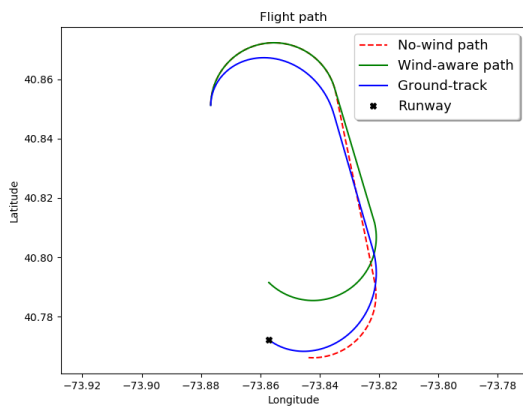


(a) 2D view.

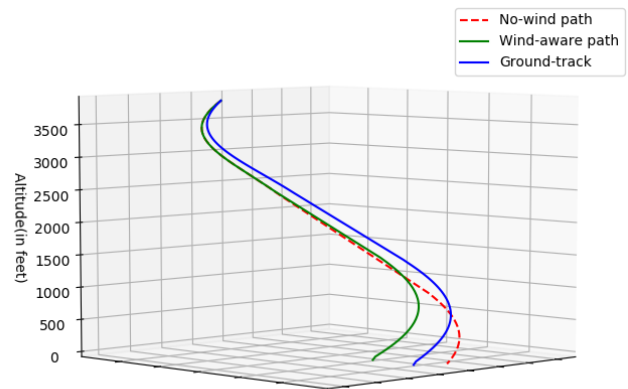


(b) 3D view.

Fig. 3.11: Wind-aware trajectory from 10000 feet in 40 knots West-wind.



(a) 2D view.



(b) 3D view.

Fig. 3.12: Wind-aware trajectory to LGA31 from 3850 feet, assisted by a 30 knots North-wind.

We also performed the following simulations loosely based on the US Airways 1549 incident, using a bank angle of 30° . We generated a no-wind air trajectory from an altitude of 10,000 feet and an initial configuration – {longitude: -73.8767, latitude: 40.8513, heading: 0.698798}, to LGA31 of La Guardia airport, New York and then implemented our wind model as described in section 3.3. For the first case, we modeled the effect of a 40 knot wind coming from North, South, East and West (Fig. 3.7). For the second case, we modeled the effect of a West-wind of 10, 20, 30 and 40 knots on the same no-wind air trajectory (Fig. 3.8).

We then generated wind-aware air trajectories to a virtual runway from altitudes of 5,000, 8,000 and 10,000 feet in the presence of a 40 knots West-wind (Fig. 3.9 - 3.11) that can lead a gliding aircraft to LGA31.

Using our wind model, we could successfully generate a wind-aware trajectory to LGA31 from an altitude of 3850 feet, assisted by a 30 knots North-wind, even though a no-wind trajectory in the same configuration was not possible (Fig. 3.12). This clearly shows the potential of the model for generating wind-aware trajectories when no-wind trajectories are infeasible.

We used a clean configuration glide ratio of 17.25:1 for straight line glide as predicted in [8] with a dirty configuration glide ratio of 9:1 for the final extended runway approaches. On an average, it took around 50 milliseconds to generate a single trajectory on an Intel Core i7-7500U CPU - 2.70GHz.

CHAPTER 4

Related Work

4.1 3D Trajectory Generation for Aircraft Using Dubins Curves

Dubins curves [10] are used to find the shortest paths, in two dimensions, between two configurations for a robot or a car that can move only in one direction. Dubins 2D shortest car paths have been previously applied for generating shortest paths for aircraft in three-dimensional space. Atkins *et al.* use Dubins paths to generate 3D trajectories for aircraft in the event of a loss of thrust emergency [11], [12]. They define worst case trajectory, direct trajectory and high altitude trajectory. Their high altitude trajectory has intermediate 'S' turns to lose excess altitude which might take the aircraft far away from the runway. In a real-life emergency scenario, pilots would prefer trajectories that allow them to lose excess altitude as close to the target runway as possible.

Owen *et al.* propose Dubins airplane paths for fixed wing UAVs with power for maneuverability [7]. They introduce three type of trajectories for low-altitude, middle-altitude and high-altitude scenarios. The low-altitude trajectory consists of a simple 3D Dubins airplane path, the high-altitude trajectory consists of spiral turns preceded by a Dubins airplane path and the middle-altitude trajectory consists of an intermediate arc that allows the aircraft to lose excess altitude. The intermediate arc requires a swift change from left to right turn or vice versa, which is a difficult and risky maneuver to perform during a loss of thrust emergency.

4.2 Wind Optimal Dubins 2D Paths at a Constant Altitude

The problem of computing optimal paths in the presence of a constant wind using Dubins paths has previously been investigated. McGee *et al.* [9] explored a method for computing shortest paths by formulating an optimization problem to find the optimal path in a two-dimensional plane. Techy *et al.* [13] described a framework for minimum-time path planning in which they characterize paths in the ground frame of reference by using kinematic equations in the trochoidal frame and derive a condition for optimality. Both approaches refined the problem of finding a valid trajectory in the presence of wind to that of intercepting

a target (the virtual runway) moving away from the actual runway in the upwind direction. However, their work was focused on trajectory planning in the two-dimensional horizontal plane for aircraft flying at a constant altitude and did not consider the change in altitude of the aircraft or its flight capabilities.

4.3 Data Streaming and Data-Driven Avionics Systems

Prior work on data-driven application for avionics systems include PILOTS – a ProgrammIng Language for spatiO-Temporal data Streaming applications which can detect sensor failures from data and estimate quantities of interest like aircraft airspeed and fuel quantity upon fault detection and isolation [14], development of failure models to detect errors in aircraft sensor data [15], simulation of error detection and correction using real data from flights [16], development of error signatures to detect abnormal conditions from aircraft sensor data and classify them [17], developing formal definition of error signatures and error recovery from sensor data [18] and programming model to reason about spatio-temporal data streams [19]. Successful implementation of PILOTS has been done using data from real-life incidents, as in the case of Tuninter 1153, where a wrong fuel quantity indicator resulted in fuel exhaustion and engine failure [20].

4.4 Improvements Over Existing Work

The main aspects where our research improves over existing work are:

- Our data-driven model can accurately consider the flight capabilities of an aircraft affected by a LOT emergency. The flight capabilities of the damaged aircraft are reflected in the inferred value of the baseline glide ratio that is computed from the sensor data during an actual emergency.
- Our algorithm removes the need for ‘S’ turns and intermediate arcs and generates trajectories which always keep an aircraft as close to the runway as possible.
- Our wind model can predict wind for trajectories with spirals and straight line segments. This allows us to generate 3D trajectories which consider the glide ratio and altitude change of an aircraft during LOT emergencies.

- In order to perform simulations using our algorithm, we developed a software written in C. The simulations were done on an Intel Core i7-7500u CPU - 2.70GHz with 8 GB of RAM, running Ubuntu 16.04 LTS. On an average, it took about 50 milliseconds to generate a single trajectory using a single bank angle as compared to the 1-2 seconds generation time in [11].

CHAPTER 5

Conclusion and Future Work

5.1 Conclusion

Augmenting flight management architectures with a system to generate and rank feasible trajectories in case of LOT scenarios will help in reducing the response time of pilots for choosing a course of action to make a successful landing in case of such emergency situations. Our evaluation of US Airways flight 1549 shows that using a baseline glide ratio of 17.25:1 for straight line flight, runways were reachable up to 28 seconds after the emergency was detected and a water landing could have been avoided if this information was made available to the pilots during the actual emergency. Our algorithm was unable to generate trajectories to Teterboro airport even though we had successfully managed to land the flight at TEB24 during simulator trials. In the case of US Airways 1549, the left engine still had 30% power. While it is not clear how much of this power turned into thrust for a damaged engine, a conservative baseline glide ratio of 19:1 illustrates that trajectories can be generated for up to 36 seconds after birds' strike.

Our experiments also clearly show that with a proper wind model, it is possible to design prediction based dynamic data-driven systems that can be used to quickly generate wind-aware trajectories in case of LOT emergencies. Furthermore, our wind model allowed us to generate wind-aware trajectories in certain cases when no-wind trajectories were not possible. This shows that considering wind in the trajectory generation phase may present new wind-assisted options or reject options rendered infeasible by wind. Trajectories computed using this approach can be guaranteed to be of the highest fidelity since they consider the capabilities of the aircraft and the wind conditions during an actual emergency. This will allow pilots to quickly decide on a reasonable course of action for safely landing an aircraft without having to manually consider the feasibility of various choices. Using a data-driven feedback loop, DDDAS based trajectory generation systems can determine the actual capabilities of the affected aircraft at the time in question and generate trajectories that are practical and reject previously calculated trajectories that might no longer be feasible. DDDAS can significantly improve the accuracy of generated flight trajectories thereby enabling better decision support systems for pilots in emergency conditions.

5.2 Future Work

Future directions of work include the implementation of variable wind gradients, which is true for real-world scenarios where the wind conditions change with a change in altitude. Designing terrain-aware algorithms that can detect obstacles and generate paths that avoid them is also an interesting direction of work. Traditional obstacle avoidance algorithms depend on graph search techniques which have a high computational time. Therefore, it is necessary to design heuristic obstacle detection algorithms that can produce accurate results in the shortest possible time. Willcox *et al.* [21] compute failure probabilities of maneuvers for aerospace vehicles. Uncertainty quantification is another possible direction of work which will help us to represent conditions such as wind speed, glide ratio, and pilot errors as probability distributions and convert them into a region of possibility around trajectories and allow us to compute the failure probabilities of trajectories.

REFERENCES

- [1] “Final Report: Accident involving ATR 72 aircraft, registration marks TL-LBB ditching off the coast of Capo Gallo (Palermo-Sicily),” Agenzia Nazionale per la Sicurezza del Volo, San Marino, Italy, 2005.
- [2] “Accident Report: Loss of thrust in both engines after encountering a flock of birds and subsequent ditching on the Hudson River US Airways Flight 1549, Airbus A320-214, N106US, Weehawken, New Jersey, January 15, 2009,” National Transportation Safety Board, Washington, DC, USA, 2010.
- [3] S. Paul, F. Hole, A. Zyteck, and C. A. Varela, “Flight trajectory planning for fixed wing aircraft in loss of thrust emergencies,” Rensselaer Polytechnic Institute, Troy, NY, USA, Tech. Rep., Oct. 2017.
- [4] F. Darema, “Dynamic data driven applications systems: New capabilities for application simulations and measurements,” in *Proc. 5th Int. Conf. Comput. Sci.*, Atlanta, GA, USA, May 2005, pp. 610–615.
- [5] S. Paul, F. Hole, A. Zyteck, and C. A. Varela, “Wind-aware trajectory planning for fixed-wing aircraft in loss of thrust emergencies,” in *Proc. 37th AIAA/IEEE Digit. Avionics Syst. Conf.*, London, England, UK, Sept. 2018, pp. 558–567.
- [6] R. F. Stengel, *Flight Dynamics*. Princeton, NJ, USA: Princeton University Press, 2015.
- [7] M. Owen, R. W. Beard, and T. W. McLain, “Implementing dubins airplane paths on fixed-wing UAVs,” in *Handbook of Unmanned Aerial Vehicles*. Dordrecht, Netherlands: Springer Netherlands, 2015, pp. 1677–1701.
- [8] K. A. Avrenli and B. J. Dempsey, “Is ”Green Dot” always the optimum engines-out glide speed on the Airbus A320 aircraft?” *J. Aviation/Aerosp. Educ. & Res.*, vol. 24, no. 3, p. 33, 2015.
- [9] T. McGee, S. Spry, and K. Hedrick, “Optimal path planning in a constant wind with a bounded turning rate,” in *Proc. AIAA Guidance, Navigation, and Control Conf. and Exhibit*, San Francisco, CA, USA, Aug. 2005, p. 6186.
- [10] L. E. Dubins, “On curves of minimal length with a constraint on average curvature, and with prescribed initial and terminal positions and tangents,” *Amer. J. Math.*, vol. 79, no. 3, pp. 497–516, 1957.
- [11] E. M. Atkins, I. A. Portillo, and M. J. Strube, “Emergency flight planning applied to total loss of thrust,” *J. Aircraft*, vol. 43, no. 4, pp. 1205–1216, 2006.

- [12] E. M. Atkins, “Emergency landing automation aids: an evaluation inspired by US Airways flight 1549,” in *Proc. AIAA Infotech@ Aerosp. Conf.*, Atlanta, GA, USA, April 2010, p. 3381.
- [13] L. Techy and C. A. Woolsey, “Minimum-time path planning for unmanned aerial vehicles in steady uniform winds,” *J. Guidance, Control, and Dynamics*, vol. 32, no. 6, pp. 1736–1746, 2009.
- [14] S. Imai and C. A. Varela, “A programming model for spatio-temporal data streaming applications,” in *Proc. Dyn. Data-Driven Appl. Syst.*, Omaha, NE, USA, June 2012, pp. 1139–1148.
- [15] S. Imai, S. Chen, W. Zhu, and C. A. Varela, “Dynamic data-driven learning for self-healing avionics,” *Cluster Computing*, vol. 20, pp. 1–24, Nov. 2017.
- [16] S. Imai, A. Galli, and C. A. Varela, “Dynamic data-driven avionics systems: Inferring failure modes from data streams,” in *Proc. Dyn. Data-Driven Appl. Syst.*, Reykjavik, Iceland, June 2015, pp. 1665–1674.
- [17] S. Imai, R. Klockowski, and C. A. Varela, “Self-healing spatio-temporal data streams using error signatures,” in *Proc. 2nd Int. Conf. on Big Data Sci. and Eng.*, Sydney, Australia, Dec. 2013, pp. 957–964.
- [18] R. Klockowski, S. Imai, C. Rice, and C. A. Varela, “Autonomous data error detection and recovery in streaming applications,” in *Proc. Int. Conf. on Comput. Sci.*, Barcelona, Spain, May 2013, pp. 2036–2045.
- [19] S. Imai and C. A. Varela, “Programming spatio-temporal data streaming applications with high-level specifications,” in *Proc. 3rd ACM SIGSPATIAL Int. Workshop on Querying and Mining Uncertain Spatio-Temporal Data*, Redondo Beach, CA, USA, Nov. 2012, pp. 18–25.
- [20] S. Imai, E. Blasch, A. Galli, W. Zhu, F. Lee, and C. A. Varela, “Airplane flight safety using error-tolerant data stream processing,” *IEEE Aerosp. and Electron. Syst. Mag.*, vol. 32, no. 4, pp. 4–17, 2017.
- [21] D. Allaire, J. Chambers, R. Cowlagi, D. Kordonowy, M. Lecerf, L. Mainini, F. Ulker, and K. Willcox, “An offline/online DDDAS capability for self-aware aerospace vehicles,” *Proc. Comput. Sci.*, vol. 18, pp. 1959–1968, 2013.